

AD-A081 076

NAVAL POSTGRADUATE SCHOOL MONTEREY CA  
PHYSICAL MODELING OF SOUND SHADOWING BY SEAMOUNTS.(U)  
SEP 79 R P SPAUDLING

F/S 20/1

UNCLASSIFIED

1 OF 1  
AD A081076



END

DATE

3-80

DDC

LEVEL II (2)

ADA 081 076

# NAVAL POSTGRADUATE SCHOOL

Monterey, California



DTIC  
ELECTRONIC  
FEB 27 1980

## THESIS

A

DDC FILE COPY

PHYSICAL MODELING OF SOUND

SHADOWING BY SEAMOUNTS

by

ROBERT PARISH SPAULDING JR.

September 1979

Thesis Advisor : H. Medwin

Approved for public release; distribution unlimited

80 2 19 108

Unclassified

SECURITY CLASSIFICATION OF THIS PAGE (When Data Entered)

REPORT DOCUMENTATION PAGE		READ INSTRUCTIONS BEFORE COMPLETING FORM
1. REPORT NUMBER	2. GOVT ACCESSION NO.	3. RECIPIENT'S CATALOG NUMBER
4. TITLE (and Subtitle) Physical Modeling Of Sound Shadowing By Seamounts		5. TYPE OF REPORT & PERIOD COVERED Master's Thesis, September 1979
7. AUTHOR(s) Robert Parish/Spaulding, Jr.		6. PERFORMING ORG. REPORT NUMBER
8. PERFORMING ORGANIZATION NAME AND ADDRESS Naval Postgraduate School Monterey, California 93940		9. CONTRACT OR GRANT NUMBER(s)
11. CONTROLLING OFFICE NAME AND ADDRESS Naval Postgraduate School Monterey, California 93940		10. PROGRAM ELEMENT, PROJECT, TASK AREA & WORK UNIT NUMBERS 12. REPORT DATE September 1979 13. NUMBER OF PAGES 84
14. MONITORING AGENCY NAME & ADDRESS (if different from Controlling Office)		15. SECURITY CLASS. (of this report) Unclassified 16. DECLASSIFICATION/DOWNGRADING SCHEDULE
16. DISTRIBUTION STATEMENT (of this Report) Approved for public release, distribution unlimited.		
17. DISTRIBUTION STATEMENT (of the abstract entered in Block 20, if different from Report)		
18. SUPPLEMENTARY NOTES		
19. KEY WORDS (Continue on reverse side if necessary and identify by block number) Acoustic Energy Diffraction Sound Shadowing		
20. ABSTRACT (Continue on reverse side if necessary and identify by block number) Propagation loss due to shadowing by seamounts is studied utilizing physical models in air. Dickens Seamount in the Gulf of Alaska is approximated by three models: a plane wedge, a contoured wedge, and a scaled three dimensional model. The forward diffraction over each is analyzed for a five octave frequency range. A new concept, the far-field "diffraction scattering strength" is defined and used to predict frequency-dependent diffraction loss at sea. The total propagation		

DD FORM 1473  
1 JAN 73  
(Page 1)

EDITION OF 1 NOV 68 IS OBSOLETE  
S/N 0102-014-6001

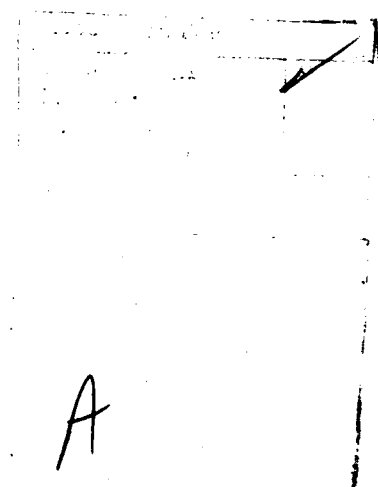
Unclassified

SECURITY CLASSIFICATION OF THIS PAGE (When Data Entered)

Unclassified

SECURITY CLASSIFICATION OF THIS PAGE/When Data Entered

loss is calculated by adding laboratory model values of upslope forward scatter and crest diffraction losses to computer-predicted ray refraction losses up to and away from the Seamount. This predicted loss is then compared to long range ocean propagation loss measurements for the case in which rays are completely blocked by the Seamount. Close agreement is found.



DD Form 1473  
1 Jan 73  
S/N 0102-014-6601

Unclassified

2 SECURITY CLASSIFICATION OF THIS PAGE/When Data Entered

Approved for public release; distribution unlimited

PHYSICAL MODELING OF SOUND SHADOWING BY SEAMOUNTS

by

Robert Parish Spaulding, Jr.  
Lieutenant, United States Navy  
B.S., University of Rhode Island, 1970  
M.S., George Washington University, 1977

Submitted in partial fulfillment of the  
requirement for the degree of

MASTER OF SCIENCE IN ENGINEERING ACOUSTICS

from the

Naval Postgraduate School  
September 1979

Author

Robert P. Spaulding

Approved by:

Edmund Rader

Thesis Advisor

O. B. Wilson, Jr.

Second Reader

William M. Tolles

Chairman, Department of Physics & Chemistry

William M. Tolles

Dean of Science and Engineering

# ABSTRACT

Propagation loss due to shadowing by seamounts is studied utilizing physical models in air. Dickens Seamount in the Gulf of Alaska is approximated by three models: A plane wedge, a contoured wedge, and a scaled three dimensional model. The forward diffraction over each is analyzed for a five octave frequency range. A new concept, the far-field "diffraction scattering strength" is defined and used to predict frequency-dependent diffraction loss at sea. The total propagation loss is calculated by adding laboratory model values of upslope forward scatter and crest diffraction losses to computer-predicted ray refraction losses up to and away from the seamount. This predicted loss is then compared to long range ocean propagation loss measurements for the case in which rays are completely blocked by the Seamount. Close agreement is found.

## TABLE OF CONTENTS

I. INTRODUCTION -----	8
II. RESEARCH FACILITIES -----	9
A. ANECHOIC CHAMBER AND DATA PROCESSING EQUIPMENT -----	9
B. STANDARD EQUIPMENT LIST -----	10
III. THEORY -----	15
IV. THE OCEAN STUDY -----	20
V. EXPERIMENTAL DESIGN & PROCEDURES -----	25
A. PHYSICAL MODELING -----	25
1. The 14° Wedge -----	25
2. The Contour Wedge -----	26
3. The Three Dimensional Model -----	28
B. SOURCE/RECEIVER SELECTION -----	32
C. SIGNAL PROCESSING -----	35
1. Source Signal -----	35
2. Received Signal Processing -----	36
VI. EXPERIMENTAL RESULTS AND ANALYSIS -----	41
A. DIFFRACTION SCATTERING STRENGTH (DDS) AND DIFFRACTION LOSS (DL) -----	41
B. COMPARATIVE DIFFRACTION BY THE MODEL -----	42
C. ACOUSTICAL SURVEY OF THE 3D MODEL -----	55
1. Sensitivity To Contour -----	55
2. Sensitivity To Position Of Ridge Crossing -----	57
3. Sensitivity To Sample Window Duration -----	66
4. Sensitivity To Azimuth -----	68

D. COMPARISON OF LABORATORY PREDICTIONS WITH AT-SEA DATA -----	68
1. Measurement Of Scattering Loss -----	70
2. Measurement Of Diffraction Loss -----	76
3. Computation Of The Refraction Losses -----	79
4. Total Propagation Loss -----	80
VII. CONCLUSIONS -----	81
BIBLIOGRAPHY -----	82
INITIAL DISTRIBUTION LIST -----	83



### ACKNOWLEDGEMENTS

The encouragement and guidance of Dr. H. Medwin of the Naval Postgraduate School is particularly acknowledged.

The computer programming of Mrs. Jeanie Savage is greatly appreciated. Special thanks are due to Mr. R. Moeller, the Department of Aeronautical Engineering, and Modelmakers, Inc. of San Francisco for construction of the models used in the experiment. The close cooperation of Mr. Gordon Ebbeson and the Defense Research Establishment Pacific (Victoria, B.C., Canada) was most helpful.

The financial support of the Office of Naval Research and ASW 13 is acknowledged.

## I. INTRODUCTION

Diffraction of acoustic energy by wedges has been theoretically investigated by a number of authors. Of particular interest is the work by Biot and Tolstoy [Ref. 17]. Their solution to a sound impulse radiated from a point source and diffracted by a rigid, infinite wedge employs the approach of normal modes and the method of normal coordinates.

Bremhorst [Ref. 27] has demonstrated close agreement between Biot-Tolstoy theoretical predictions and experimental data using a  $90^\circ$  wedge as the diffracting barrier.

The question now is whether this predictive ability can guide the prediction of forward diffraction by more complex, real-world barriers. Specifically, can diffracted sound energy be predicted in the shadow zone of a seamount or underwater ridge?

To accomplish this purpose, three barriers were constructed: a simple plane wedge, a long-crested (two-dimensional) wedge contoured to an at-sea sound track, and a three dimensional model of a seamount. Acoustic energy was diffracted over each in order to determine "diffraction scattering strength", a newly defined concept, and "diffraction loss". This was in turn compared to at-sea data showing the effects of shadowing on sound propagation by the Dickens Seamount in the Gulf of Alaska. The results of this study indicate that the diffracted energy over complex barriers can be predicted utilizing physical laboratory models.

## II. RESEARCH FACILITIES

### A. ANECHOIC CHAMBER AND DATA PROCESSING EQUIPMENT

The experiments were conducted in the Naval Postgraduate School (air) anechoic chamber, providing superb isolation from excess background noise, and a very stable medium for sound travel.

Data acquisition and processing were accomplished using a digital computer system composed of four major components interfaced to provide high speed analog to digital conversion, digital processing and data printout. The design was developed by the Special Projects section of Naval Air Development Center in conjunction with Pinkerton Computer Consultants, Inc. of Warminster, Pennsylvania. The major components are:

#### 1. Interdata Model 70 Computer

This minicomputer is a digital design that is FORTRAN and Basic programmable with a 64 thousand byte memory. Data that have been stored on floppy discs can be read into the computer for processing. There is an identical capability utilizing cassette tapes.

#### 2. Phoenix Analog to Digital Converters, Model ADC 912

Two ADC 912 analog to digital converters may be used separately or simultaneously. Each converter is a very high speed, high accuracy device capable of encoding  $\pm 10$  volt input signals into twelve binary bits of data with a resolution limit of one part in 4,095 at a maximum time of

2 microseconds per conversion. It measures the input voltage against an internal precision reference voltage with an accuracy of  $\pm 0.025\%$  of full scale. The ADC 912's will accommodate a typical commutating through-put rate of 476,190 channels per second, including settling time. The sampling frequency is set in a stable frequency synthesizer and sent to the converter via a sampling circuit.

3. Texas Instruments Silent Electronic Data Terminal, Model 733

The TI 733 consists of a key board used as a programming input/output control device, a printer, and a transmit/receiver mechanism going to a peripheral disc drive unit. The overall system facilitates rapid, accurate processing of any desired type of analog electrical signal and was used primarily for frequency domain analyses using standard FFT algorithms.

B. STANDARD EQUIPMENT LIST

The following scientific equipment was utilized to conduct the experimental work:

Interface Technology Timing Simulator/Word Generator, Model RS-648

Tektronix Type 545B Oscilloscope with four trace plug-in

General Radio Type 1163-A Coherent Decade Frequency Synthesizer

Hewlett-Packard Electronic Counter, Model 5223L

Hewlett-Packard DC Power Supply, Model 721A (two)

E&L Instruments DD-1 Digi Designer

Hewlett-Packard Dual-Trace Oscilloscope, Model 140A

Fluke True RMS Voltmeter, Model 8920A

Fluke Digital Multimeter, Model 8000A

Hewlett-Packard Power Amplifier, Model 467A

Wavetek Arbitrary Waveform Generator, Model 175

Lambda Regulated Power Supply

Krohn-Hite Frequency Filter, Model 3550 (two)

Princeton Applied Research Amplifier, Model 113 (two)

Bruel and Kjaer Type 4145 Condenser Microphone

Bruel and Kjaer Type 4134 Condenser Microphone

Bruel and Kjaer Microphone Power Supply, Model 2804

The equipment diagram for the experiment is shown in  
Figure 3.

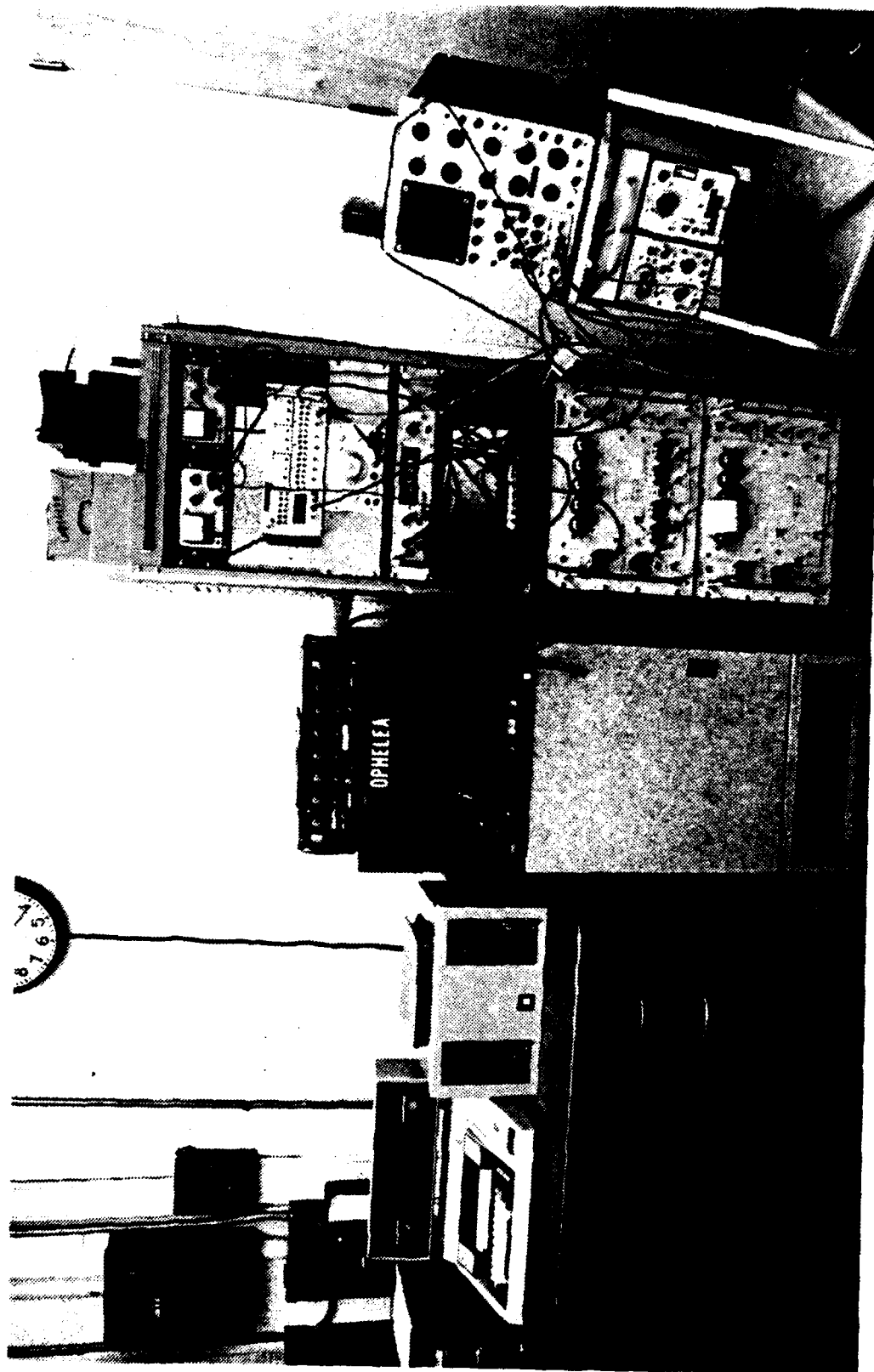


Figure 1. Laboratory Computer System

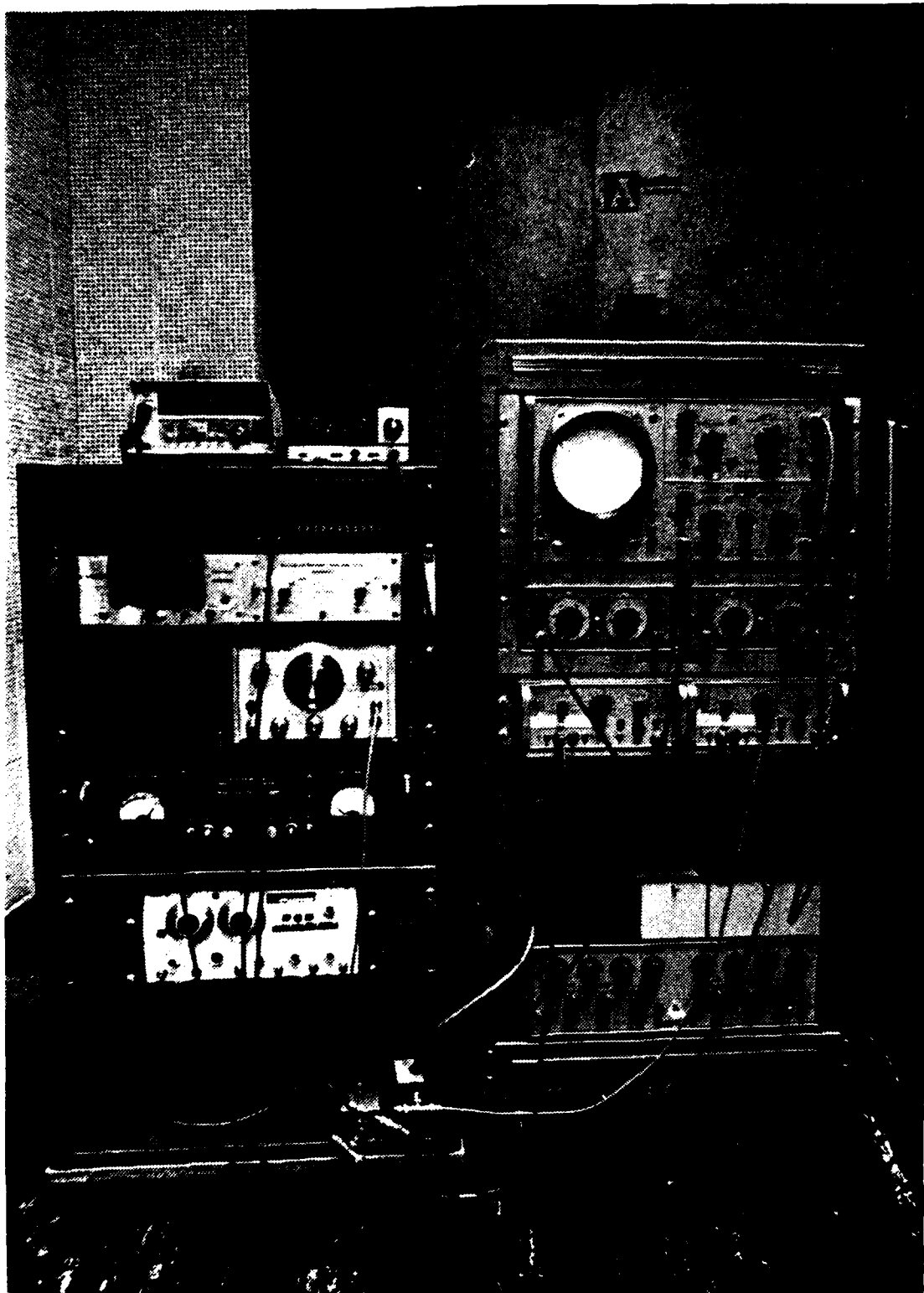


Figure 2. Typical Rack Mounting

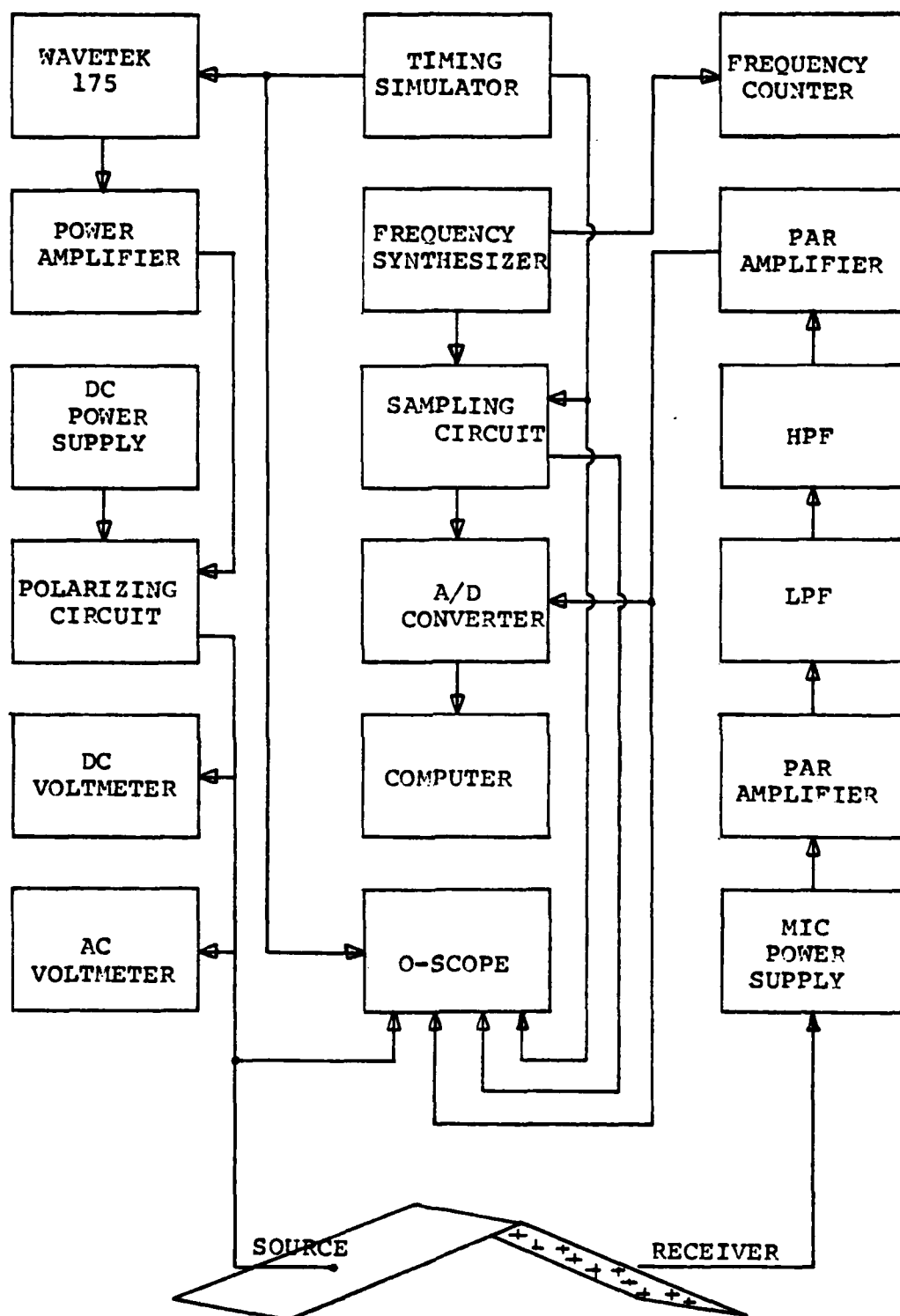


Figure 3. Equipment Diagram



### III. THEORY

Diffraction can be generally described as a phenomenon which occurs whenever a wavefront encounters an obstacle. To examine the process theoretically, consider an infinite wedge which is bounded by rigid plates at  $\theta = 0$ ,  $\theta = \theta_w$  and intersecting along the z-axis or apex. The region is occupied by a homogeneous compressible fluid of sound velocity  $c$  and density  $\rho$ .

To determine the normal modes of the system, it is convenient to solve the acoustic wave equation in cylindrical coordinates, in terms of the displacement potential  $q$ :

$$\frac{\partial^2 q}{\partial r^2} + \frac{1}{r} \frac{\partial q}{\partial r} + \frac{1}{r^2} \frac{\partial^2 q}{\partial \theta^2} + \frac{\partial^2 q}{\partial z^2} = \frac{1}{c^2} \frac{\partial^2 q}{\partial t^2} \quad (1)$$

The harmonic solutions to this equation are of the form

$$q = e^{\pm i\nu\theta} H_{\nu}^{(1,2)}(Kr) e^{\pm i\gamma z} e^{\pm i\omega t} \quad (2)$$

where

$$\gamma^2 = \frac{\omega^2}{c^2} - K^2 \quad (3)$$

The rigid plates of the wedge establish boundary conditions such that:

$$\frac{\partial q}{\partial \theta} = 0 \quad \text{at} \quad \theta = 0, \theta = \theta_w \quad (4)$$

Consequently,

$$q = \cos \nu_n \theta H_{\nu}^{(1,2)} e^{\pm i\gamma z} e^{\pm i\omega t} \quad (5)$$

and

$$\nu_n = \frac{n\pi}{\theta_w} \quad (6)$$

At  $r=0$ , the imaginary part of the Hankel function becomes infinite which is not physically realizable. Therefore, only the real parts of  $H_\nu^{(1,2)}$ , the Bessel functions of the first kind, will be kept.

At this point, assume an explosive point source at  $r=r_0$ ,  $\theta = \theta_0$ , and  $z=0$ . This will result in solutions to equation (5) which are symmetric in the  $z$ -axis. Biot and Tolstoy now apply normal coordinate methods. For an in depth look at the mathematics of the solution technique, see Refs. 1 and 3. Leaping directly to the results, the solution form to equation (1) becomes:

$$\frac{\partial q}{\partial t} = -\frac{c}{\theta_w} \sum_n \cos \nu_n \theta \cos \nu_n \theta_0 I_n, \quad ct \geq z \quad (7)$$

where 
$$I_n = \int_0^\infty J_{\nu_n}(Kr) J_{\nu_n}(Kr_0) J_0[K(c^2 t^2 - z^2)^{1/2}] K dK \quad (8)$$

A transform given in Appendix X, Ref. 3 may be used to reduce  $I_n$  to more physically visualizeable terms. Letting

$$t_0 = \frac{1}{c} [(r-r_0)^2 + z^2]^{1/2} \quad (9)$$

$$\hat{t}_0 = \frac{1}{c} [(r+r_0)^2 + z^2]^{1/2} \quad (10)$$

$t_0$  is the time required for a sound pulse to travel directly from source to receiver in the general case.  $\hat{t}_0$  is the time required to travel from source to wedge apex to receiver, ie., the diffracted energy path. As a result, equation (8) will have three solutions:

for  $t < t_0$ ,  $t_0 < t < \hat{t}_0$ , and  $\hat{t}_0 < t$ . Since this work is confined to studying the energy only in the shadow zone of a barrier, only the solution involving the diffracted wave,  $\hat{t}_0 < t$ , is of interest.

For this case

$$I_n = \frac{-1}{\pi r r_0 \sinh y} \sin \nu_n \pi e^{-\nu_n y} \quad (11)$$

$$\text{where } y = \text{arc cosh } \frac{c^2 t^2 - (r^2 + r_0^2 + z^2)}{2 r r_0} \quad (12)$$

Now combining with equation (7)

$$\frac{\partial Q}{\partial t} = \frac{c}{\pi a_w} \frac{1}{r r_0 \sinh y} \sum_n \cos \nu_n \theta_0 \cos \nu_n \theta \sin \nu_n \pi e^{-\nu_n y}, \quad \hat{t}_0 < t \quad (13)$$

Rewriting the trigonometric functions in terms of their exponential identities and then collecting the conjugate pairs together, equation (13) becomes

$$\frac{\partial Q}{\partial t} = \frac{c}{4\pi a_w} \frac{1}{r r_0 \sinh y} e^{-\frac{\pi y}{a_w}} \left[ \frac{\sin\left(\frac{\pi}{a_w}\right)(\pi \pm \theta \pm \theta_0)}{1 - 2e^{-\frac{\pi y}{a_w}} \cos\left(\frac{\pi}{a_w}\right)(\pi \pm \theta \pm \theta_0) + e^{-\frac{2\pi y}{a_w}}} \right] \quad (14)$$

For the unit impulse source used in Refs. 1 and 3 the displacement potential  $Q$  is related to the acoustic pressure by

$$p = -\rho \frac{\partial^2 Q}{\partial t^2} \quad (15)$$

If, on the other hand, one assumes a source that is a delta function in time as well as space, the acoustic pressure due to the diffracted wave alone, ie., in the shadow region of a wedge is given by

$$p = \frac{-\rho c}{4\pi a_w} \frac{1}{r r_0 \sinh y} e^{-\frac{\pi y}{a_w}} \left[ \frac{\sin\left(\frac{\pi}{a_w}\right)(\pi \pm \theta \pm \theta_0)}{1 - 2e^{-\frac{\pi y}{a_w}} \cos\left(\frac{\pi}{a_w}\right)(\pi \pm \theta \pm \theta_0) + e^{-\frac{2\pi y}{a_w}}} \right] \quad (16)$$

where

$$y = \text{arc cosh} \frac{c^2 t^2 - (r^2 + r_0^2 + z^2)}{2rr_0}$$

and

$\theta_w$  = fluid filled region above the wedge

$\theta_s$  = angle between the wedge side and the source

$\theta$  = angle between wedge side and the receiver

$r_0$  = distance from source to wedge apex

$r$  = distance from wedge apex to receiver

$z$  = distance out from the least time travel path along the wedge apex

Figure 4 illustrates the typical geometry of the problem.

The diffraction process may be described in the following manner. A point source at a distance  $r_0$  from the wedge apex is transmitting an expanding spherical wavefront. The wavefront first arrives at the apex along the least time travel path, at time  $t = r_0/c$ . The wavefront then continues to arrive at progressively later  $t$  with increasing distance  $z$ . This has the effect of establishing a series of sources along the apex which then reradiate into the shadow zone on the receiver side of the wedge. The apex of the wedge is essentially acting as a line source with time shading along the line.

Equation (16) has been transformed to the frequency domain by Medwin [Ref. 4] and used to compute theoretical values which were compared to experimental data from a simple wedge [Ref. 2].

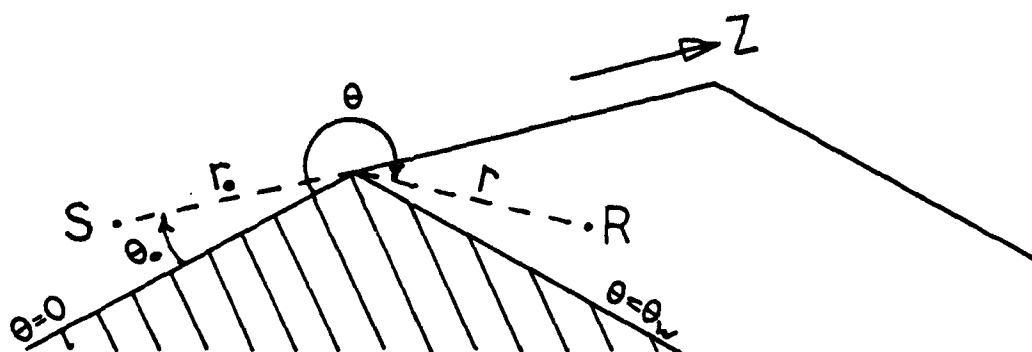


Figure 4. Typical geometry on a simple wedge.

The source is at  $r = r_0$ ,  $\theta = \theta_0$ , and  $z = 0$ . Receiver is at distance  $r$  from the wedge apex at angle  $\theta$ . The case  $\theta_0 = 0$  and  $\theta = \theta_w$  describes both source and receiver on the wedge surface.

#### IV. THE OCEAN STUDY

To determine whether the magnitude of the diffracted energy could be predicted of course required some real-world data to which experimental data could be compared. To this end, a study of shadowing of sound propagation by a seamount conducted by Ebbeson, et al. [Ref. 5] was ideally suited.

A series of propagation runs at a frequency of 230 Hz were made by Ebbeson et al. at the Dickens Seamount to determine the degree of shadowing and its effect on sound propagation. To be expected, the sound source depth played an important part in the shadowing effect due to its relative proximity to a sound channel. But particularly for a shallow source where most of the sound rays are deeply refracted, there was a significant effect on propagation loss when compared to predicted values. With source and receiver separation appropriately spaced, it was possible to have a major (15 dB) shadowing of acoustic energy when the deeply refracted rays totally impinged upon the slope of the seamount. See Figure 5 for an illustration of the ray paths. It can be seen that at ranges of 79 and 119 km maximum shadowing should take place since the source is in a position which enables the seamount to intercept the deeply refracted rays. Minimum shadowing is expected when the source is at 99 km range.

Figure 6 illustrates the measured propagation loss along with that predicted by the FACT ray propagation ray

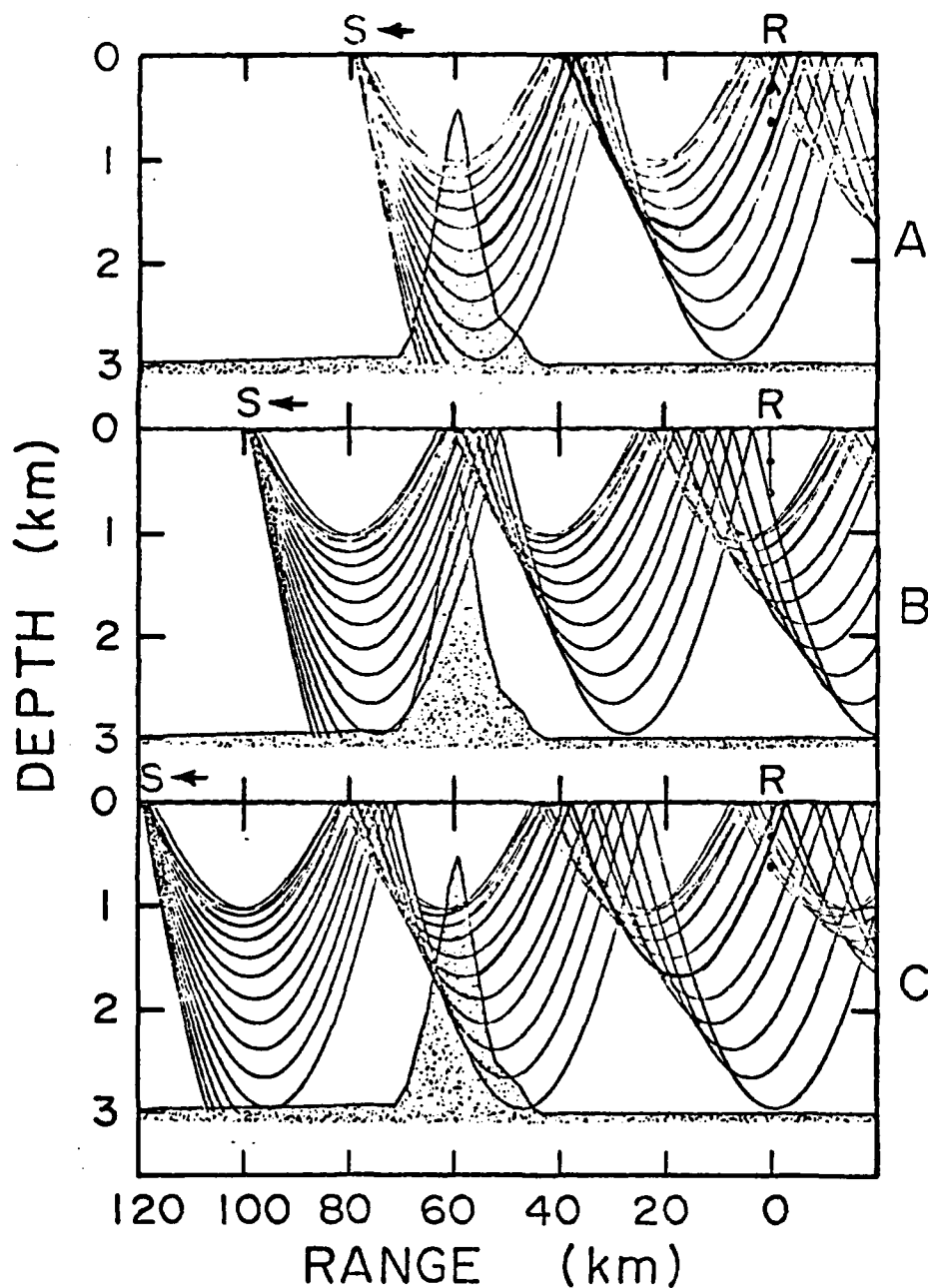


Figure 5. Ray traces for track 6. Source ranges are 79 km (A), 99 km (B), and 119 km (C). Source depth = 18 m, receiver depths = 329 m, 633 m. The source angles are  $\pm 15^\circ$  in  $1^\circ$  increments (from Ref. 5).

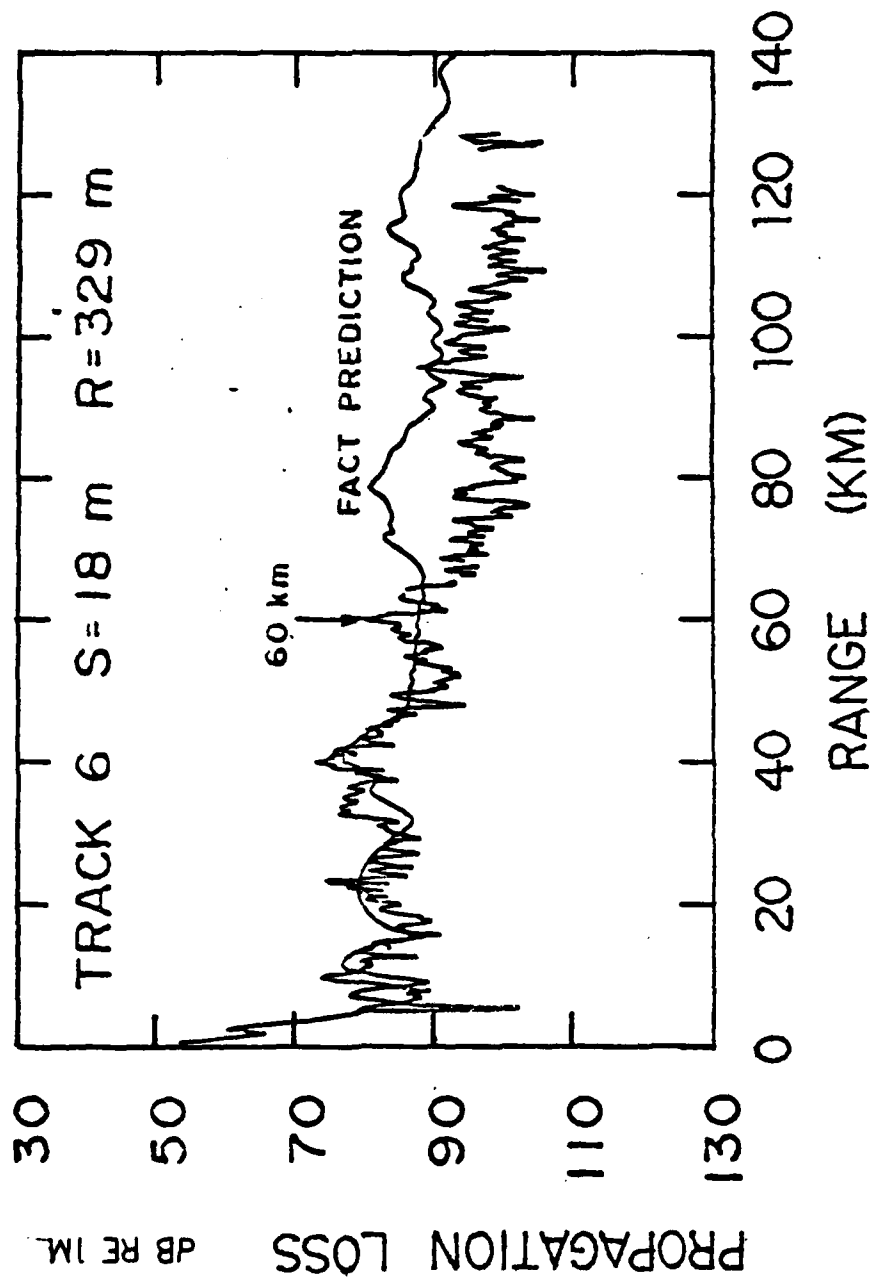


Figure 6. Measured propagation loss for track 6 with the source at 18 m and receiver at 329 m. The smooth line is the FACT prediction based on a flat bottom. The arrow indicates the seamount range (from Ref. 5).



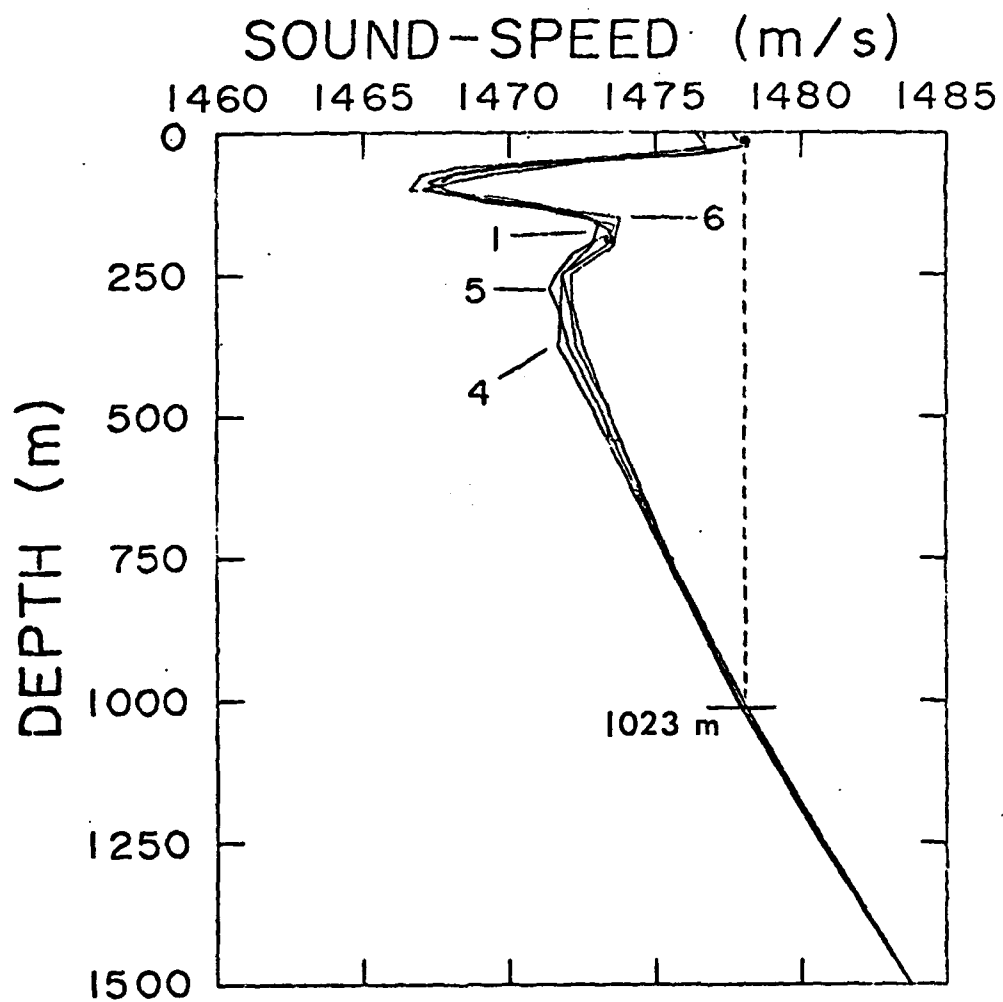


Figure 7. Average sound speed profile. Track 6 is indicated (from Ref. 5).

model. This is based on an average sound speed profile shown in Figure 7. The measured results agree well with prediction up until the point at which the source passes over the apex of the seamount (60 km). From there on the increase in propagation loss due to the shadowing effect of the seamount is apparent. At A and C there is approximately a 15 dB increase in propagation loss.

This increase in propagation loss is here postulated to be due to diffraction. The objective of this work is the prediction of the ocean diffraction loss by physical modeling in the laboratory.

## V. EXPERIMENTAL DESIGN AND PROCEDURES

### A. PHYSICAL MODELING

To physically model the Dickens Seamount several orders of approximation were used. Three models were built, each of which progressed to a new stage of complexity. The models were required to appear as having infinite dimensions when compared to the wave length of the sound signal. This was done by ensuring that the edges of the model are sufficiently far away from the receiver so that a single cycle pulse at the lowest frequency could be received without interference from edge diffraction. Therefore, with sufficiently large model dimensions in conjunction with a pulsed signal technique, the models were considered infinite for the frequency band in which the experiment was conducted. Furthermore, it was desired that the model surfaces approximate a perfectly rigid condition.

#### 1. The 14° Wedge

The first model and the simplest was constructed on the assumption that the seamount behaves acoustically as if it were a simple, geometric wedge. That is, for this model it is assumed for simplicity that the peripheral portions of the seamount make little contribution to the diffraction process and the major effects are along or close to the least time travel path. Additionally, along that travel path there is an average plane upslope and plane downslope.

Therefore, a simple plane wedge was constructed to correspond to a particular track across the seamount. Referring to Figure 8, this is track 6 of the ocean experiment [Ref. 57]. The average upslope and downslope measured with the horizontal is  $14^\circ$  so this is appropriately named the " $14^\circ$  wedge". It was made of two pieces of  $1/4$ " thick aluminum each 1.52 m (5 ft.) long by 0.6 m (2 ft.) wide and joined at the apex to make a  $152^\circ$  interior angle ( $\theta_w = 212^\circ$  in the notation of Ref. 1). Aluminum was chosen as the building material due to its rigidity and its reflection coefficient of almost unity.

## 2. The Contour Wedge

The next level in modeling complexity was to go a step beyond the concept of an average slope and to account for a contour. Therefore, the wedge was given a smoothly varying contour approximation to that of the actual seamount along track 6. Acoustically, the wedge still appeared infinite but the wavefront had to interact with a variable sloped surface rather than a flat plane on each side of the wedge apex. The contour did not vary with respect to the z-axis.

To construct this "contour wedge", as it was called, the technique resembled that used in aircraft wings. Four  $1$ " x  $12$ " pieces of lumber were cut conforming to the track 6 contour. These in turn were fastened by their flat sides to a  $3/4$ " plywood base. Then  $.040$ " thick sheet aluminum was laid over the  $1$ " x  $12$ " formers and fastened with

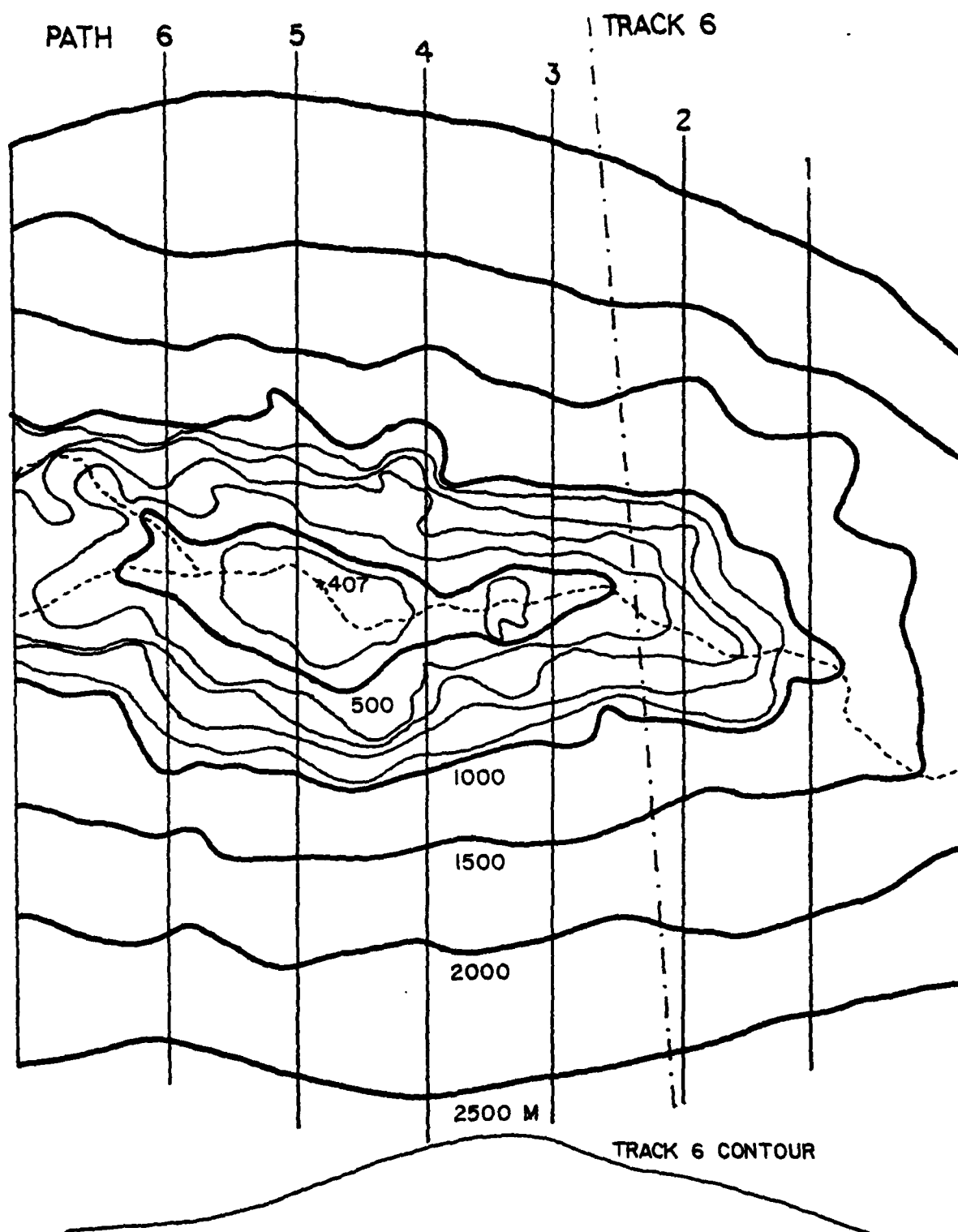


Figure 8. Contour map of the modeled area of Dickens seamount. Paths 1 through 6 represent least time travel paths at 25 cm (2 km) spacing utilized in the laboratory acoustical survey.

countersunk screws making the surface of the contour wedge. Aluminum was again used for its reflection coefficient and workability. The underside of the aluminum surface had to be coated with asphalt roofing compound to add rigidity and dampen out unwanted vibration in the presence of sound. The contour wedge was 1.83 m (6 ft.) wide by 1.22 m (4 ft.) long (in the z-axis).

### 3. The Three Dimensional Model

The final stage of complexity was a three dimensional model of the seamount. The Defense Research Establishment Pacific (Victoria, B.C., Canada) provided superbly detailed bathymetric data from which the 3D model of Dickens was constructed.

The at-sea experiment was done using a frequency of 230 Hz. To duplicate the experiment in air required either higher frequencies than the A/D converter could handle or a larger model size than could be accommodated by the entrance door to the anechoic chamber. As a compromise, the 3D model base was made approximately 2.13 m (7 ft.) square. The scale was  $1/2" = 100 \text{ m}$ . Because of the change of medium this is equivalent to 1:7874. When irradiated with sound of frequency 100 kHz in air, the model represented a frequency of 55 Hz. in water at Dickens.

The 3D model was constructed by laminating  $1/8"$  layers of particle board onto a  $1/2"$  particle board base. Each layer was cut from a properly scaled blow-up drawing of the bathymetric data with constant depth contour lines

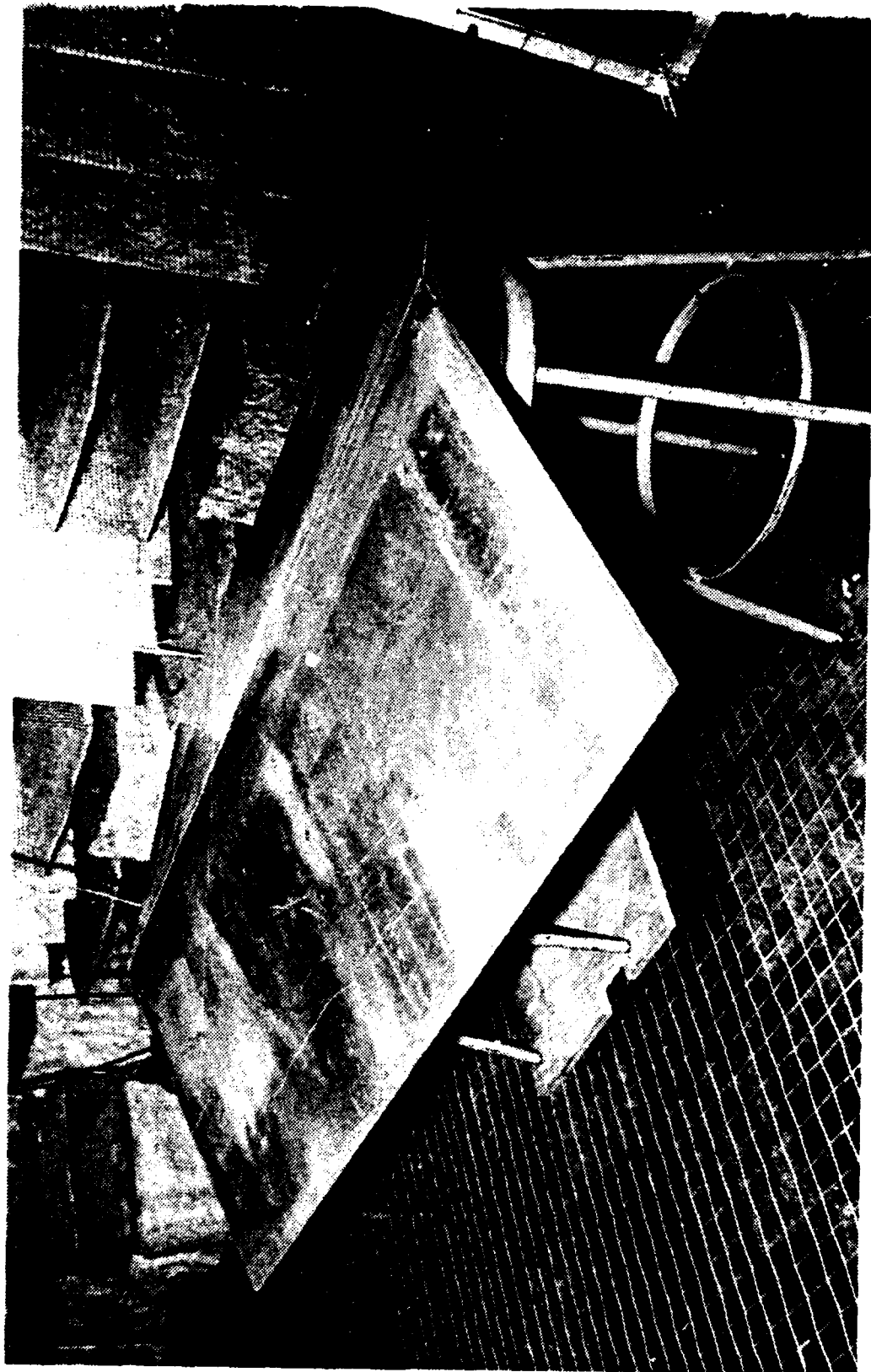


Figure 9. The  $14^{\circ}$  Wedge

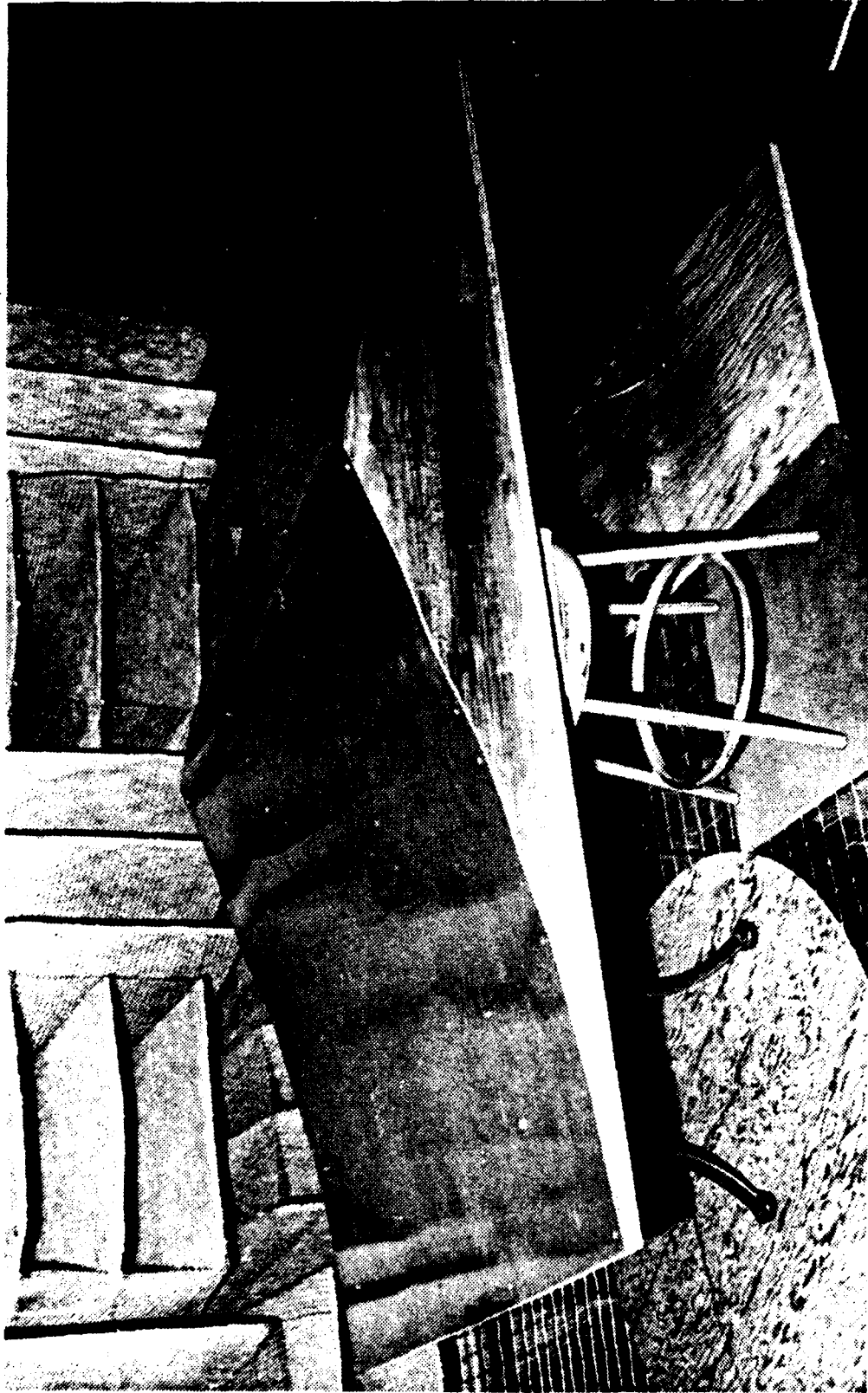


Figure 10. The Contour Wedge



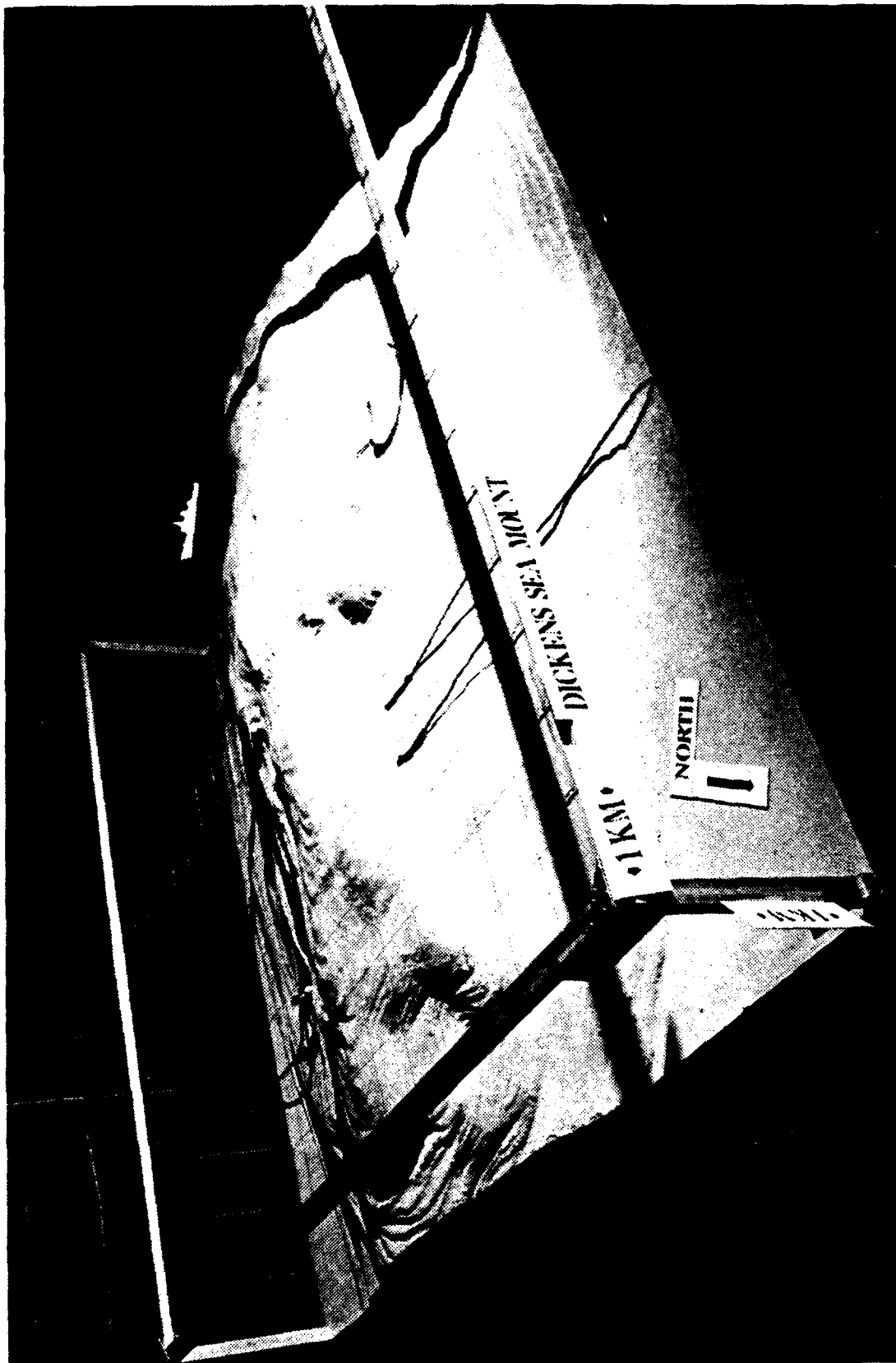


Figure 11. The 3D Model

to a depth of 2500 m marked in. This technique resulted in a depth resolution on the 3D model equivalent to 25 m at sea. Once the layering was complete, the entire model surface was coated with a thin layer of plaster to fill in the steps between each layer of particle board and to give the surface a smooth appearance. The combination of particle board and plaster was of sufficient density to result in an acoustically rigid reflector. The builder was Model-makers, Inc. of San Francisco.

#### B. SOURCE/RECEIVER SELECTION

To fulfill the conditions of the Biot-Tolstoy Wedge Theory which guided this work, it is desirable to have an approximation of a point source to transmit spherical waves. This requires that the source must be small compared to the wavelength of the transmitted signal. This condition is met if  $ka \ll 1$  where  $k$  is the wave number and  $a$  is the radius of the sound source. Additionally it is required that the radial distance from the source to the apex of the barrier be much greater than  $\lambda$ .

With the above in mind, the selection of a sound source becomes one of compromise. To achieve the closest approximation to a point source requires the smallest possible radiator; however, this also limits the maximum acoustic pressure that can be generated.

Bremhorst was confronted with the same problem of source selection and ran extensive studies to determine the optimum

radiator subject to the above constraints. He determined that the best solution was to utilize the reciprocal transducer properties of small condenser microphones and employ them as sound sources.

Likewise for this work, Bruel and Kjaer (B&K) condenser microphones were put to the task of acting as the sound source. These microphones, although being piston radiators, do have the fundamentally important property of radiating a spherical diverging wave but have a directivity term involved. This directivity factor is rendered insignificant by aiming the microphone at the barrier apex and ensuring the maximum response axis is along or very close to the least time travel path between source and receiver.

Laboratory testing was performed using the 1", 1/2", and 1/4" B&K microphones. It was found that only the 1" B&K, Type 4145, had a sufficient acoustic pressure output at 100 kHz to be used. This requirement for the maximum acoustic pressure attainable was particularly evident when transmitting sound over the 3D model because of the undulations along the sound path which caused some secondary scatter adding to the transmission loss. See Figure 12 for an illustration of the theoretical acoustic output of the various B&K microphones.

The selection of a receiver was again a matter of compromise. In this case the trade off was between trying to use the smallest microphone possible to ensure good high frequency response but at the same time preserving a sufficiently high sensitivity level. It was determined that the

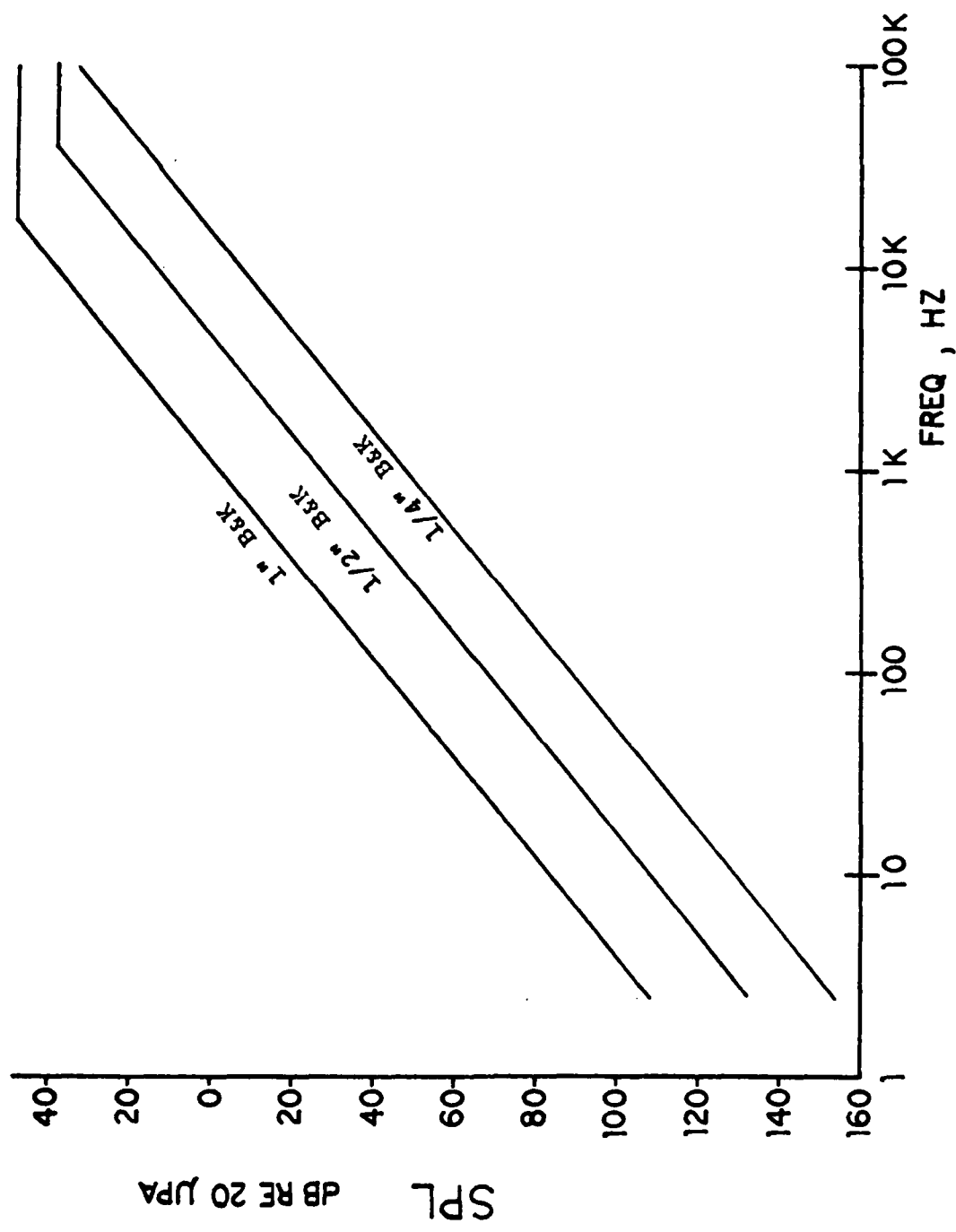


Figure 12. Theoretical sound pressure levels generated at 1 m distance for 1 volt input. (from Ref. 6)

1/2" B&K, Type 4134, was the best choice, with selection being primarily based on a useable sensitivity level. Experiments were also run to determine if a 4 mm I.D. probe could also be used with the microphone to improve high frequency performance. Based on typical pulse lengths of 400 microseconds, a 7 cm probe was required to prevent interference from reflected energy of the probe tip. Unfortunately, the probe resulted in too great a loss in acoustic pressure reaching the receiving microphone and therefore could not be used.

In the case of both the source and receiver, they were of sufficiently small size to still meet the requirement of approximately a point source, at least for the lower frequencies utilized in the experiment.

#### C. SIGNAL PROCESSING

##### 1. Source Signal

The transmitted acoustical signal waveform must consist of many frequencies so that the analysis of received data can cover a broad spectrum in the frequency domain. This was achieved by using a triangular waveform. It has a sharp positive going pulse which acts as an impulse and, when transformed to the frequency domain, provides frequencies at every harmonic of the fundamental. The harmonic amplitude spectrum is at 6 dB per octave.

To generate this waveform the Wavetek Model 175 Arbitrary Waveform Generator was utilized. With the ability to program the desired waveform plus a rise-time of 500 ns,

it is an ideal frequency generator for the experiment. The short rise time makes a good approximation of the infinite slope of an impulse.

The output signal of the waveform generator was pulsed to provide the ability to selectively sample only the diffracted signal and to eliminate any interference caused by reflections from surrounding structures. Data were collected using one cycle of the triangular waveform. Triggering of the waveform generator to provide each sent pulse was accomplished by the Interface Technology Model RS-648 timing simulator.

## 2. Received Signal Processing

After the diffracted acoustic signal was received by the 1/2" B&K microphone, it was amplified, band pass filtered to eliminate low frequency noise and prevent aliasing, and then amplified again for a total gain of 46 dB. The amplifiers used were PAR model 113 preamps due to their very low self-noise characteristics. This signal was then sent to the Phoenix A/D converter for digitizing.

To separate the diffracted signal, a sampling window was used. This was accomplished by the Interface Technology timing simulator which triggered open a sampling circuit to coincide with the beginning of the diffracted signal. This sampling window could then be left open for any predetermined time, then shut. This technique gates out any unwanted signal with 100 nanosecond accuracy.

The sampling circuit was built primarily with IC devices, associated power supplies, and an oscillator. A schematic of the circuit is illustrated in Figure 13. A general Radio Model 1163-A Decade Frequency Synthesizer was used to deliver the sampling frequency. Since it has the stability characteristics of a crystal oscillator, it provided a constant frequency to the A/D converter thereby increasing the accuracy and repeatability of the data analysis. The sampling circuit works in the following manner. The frequency synthesizer puts out a constant frequency sine wave. The sine wave is fed to a LM710CN voltage comparator which changes it to a square wave required by the A/D converter. Since the frequency synthesizer was not triggerable, a 74123N retriggerable monostable multi-vibrator was used to gate open and closed the sampling window. The timing simulator provided the trigger signal, coinciding with the beginning of the diffracted signal, to bring the "one shot" to a high, or on state. By then adjusting a variable resistor in series with a capacitor, the high state could be extended to the desired length before dropping back to low. This procedure established the sampling window. Simultaneously, the high state of the "one shot" and the square wave output of the voltage comparator were fed to a DM5411N AND gate. The output of the AND gate was a train of rectangular pulses, only for the duration of the sampling window, and sent to the A/D converter. These pulses in turn triggered the A/D converter

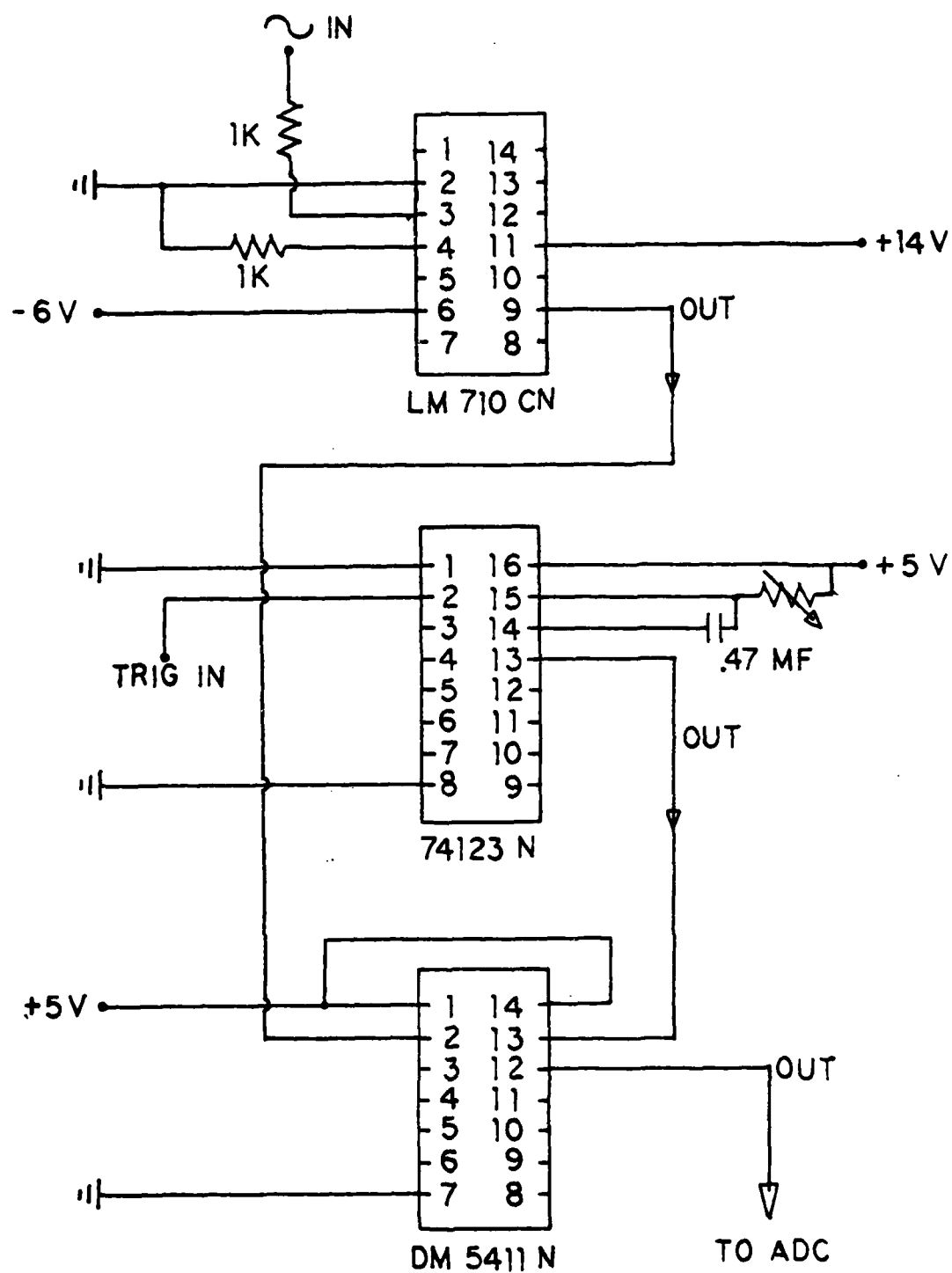


Figure 13. Sampling Circuit



to sample the analog signal. Each rectangular pulse corresponded to one-half the period of the sampling frequency set on the frequency synthesizer.

The number of samples gathered by the A/D converter in each sampling window was set to be a power of two, i.e., 64, 128, 256, etc. This was required by the FOURONE FFT algorithm which was being used to do the frequency domain analysis. The sampling frequency was set at an integral multiple of the frequency of the sent signal. Due to the excellent frequency stability characteristics of the frequency synthesizer and the Wavetek 175, this relationship could be precisely controlled thereby minimizing any truncation of the sampled waveform and eliminating sidelobes.

To further improve the quality of the information being digitized and submitted for Fourier analysis, an averaging routine, performed by software, was employed. The data from as many as 9,999 sampling windows could be averaged prior to performing the FFT; however, only 1,000 windows were normally used. This improved the signal-to-noise ratio by  $10 \log N$  where  $N$  is the number of windows averaged. If  $N = 1,000$ , this means a 30 dB improvement in signal-to-noise ratio.

The experiment was originally begun using a 2.5 kHz fundamental triangular waveform as the transmitted signal. On the receiving end, 1,000 windows, each of 400 microseconds duration, and each containing 128 samples were time averaged

prior to submission to the FFT algorithm. This resulted in satisfactory data on the diffracted sound behavior up to approximately 70 kHz. However, as indicated earlier, this behavior must be extrapolated to 430 kHz. To get more energy into the higher frequencies, it was decided to run the sound source at near its resonance frequency which is approximately 10kHz. Consequently, the experiment was continued using a 10 kHz fundamental triangular waveform which extended the satisfactory results to 100 kHz.

## VI. EXPERIMENTAL RESULTS AND ANALYSIS

### A. DIFFRACTION SCATTERING STRENGTH (DSS) AND DIFFRACTION LOSS (DL)

In dealing with underwater acoustic behavior it has always been convenient to specify the scattering characteristics of objects in decibels. For example, in the sonar literature "target strength" (TS) is used to give a decibel measure of the amount of backscatter assuming spherical radiation from the source and spherical reradiation from the target. In algebraic terms

$$TS = 20 \log \left[ \frac{P_{bs}}{P_o} \frac{R^2}{R_o R_1} \right] \quad (17)$$

where

$P_{bs}$  = backscattered acoustic pressure

$P_o$  = reference pressure

$R_o = R_1$  = reference distances

For the case of diffraction it is desirable to apply a similar universal concept. If one considers the reradiated acoustic energy from a wedge as scatter, then it is appropriate to define the decibel measure of that scatter as "diffraction scattering strength" (DSS).

Clearly, equation (17) must be modified by changing  $P_{bs}$  to a term which describes the pressure due to the diffracted wave alone, i.e.,  $P(\theta_o, \theta, \theta_w, r_o, r)$ . With respect to the

work being reported here, it is also necessary to be able to scale the DSS from water to experiments in air. To accomplish this Medwin [Ref. 4] defines the DSS to be:

$$DSS = 20 \log \left[ \frac{P(\theta_o, \theta, \theta_w, r_o, r)}{P_o} \frac{r_o}{R_o} \sqrt{\frac{r}{\lambda}} \right] \quad (18)$$

where

$$r_o = r$$

$$R_o = \text{LM reference distance}$$

$$\lambda = c/f$$

Equation (18) is dimensionless and accounts for spherical divergence from a second source, followed by cylindrical divergence after diffraction over the wedge apex. Furthermore, for a wedge, the equation gives the same value for air or water. It has been shown [Ref. 4] that the DSS becomes only a function of  $\theta_o$ ,  $\theta$ , and  $\theta_w$  provided the ranges are equal and sufficiently large, i.e.,  $r = r_o > \lambda$ .

The decibel measure of "diffraction loss" may be defined as:

$$DL = -20 \log \left[ \frac{P(\theta_o, \theta, \theta_w, r_o, r)}{P_o} \right] - 20 \log \left[ \frac{r_d}{R_o} \right] \quad (19)$$

where  $p_o$  = reference pressure and  $r_d$  is direct distance to receiver. From equation (18)

$$20 \log \left[ \frac{P(\theta_o, \theta, \theta_w, r_o, r)}{P_o} \right] = DSS - 20 \log \left[ \frac{r_o}{R_o} \sqrt{\frac{r}{\lambda}} \right] \quad (20)$$

Therefore; the diffraction loss becomes

$$DL = -DSS + 20 \log \left[ \frac{r_0}{R_0} \sqrt{\frac{r}{\lambda}} \right] - 20 \log \frac{f_d}{R_0} \quad (21)$$

For the results which follow, equations (18) and (21), giving diffraction scattering strength and diffraction loss respectively, are applied to the experimental data.

#### B. COMPARATIVE DIFFRACTION BY THE MODELS

The diffracted pressure fields in the shadow regions of the three models were studied first to quantify their differences. The  $14^\circ$  wedge provided baseline data with which data from the more complex models could be compared. Also, it provided a quick experimental verification of the Biot-Tolstoy theory transformed to frequency space for a shallow sloped wedge.

With the source positioned at  $\theta_0 = 0$  and  $r_0 = 25, 35,$  and  $45$  cm, the receiver distance  $r$  was kept equal to  $r_0$  and  $\theta = \theta_w$ .

On the 3D model, the source/receiver position was along track 6 [Ref. 57]. The decibel measure of the diffracted acoustic pressure was used to compute the diffraction scattering strength. These separate results are illustrated graphically in Figure 14 through 22. The theoretical DSS, determined from the Biot-Tolstoy theory, is also plotted along with the experimental DSS of the  $14^\circ$  wedge and shows very good agreement.

Figure 23 gives a good synopsis of the results. Note that the DSS for the  $14^\circ$  wedge remains at a relatively constant

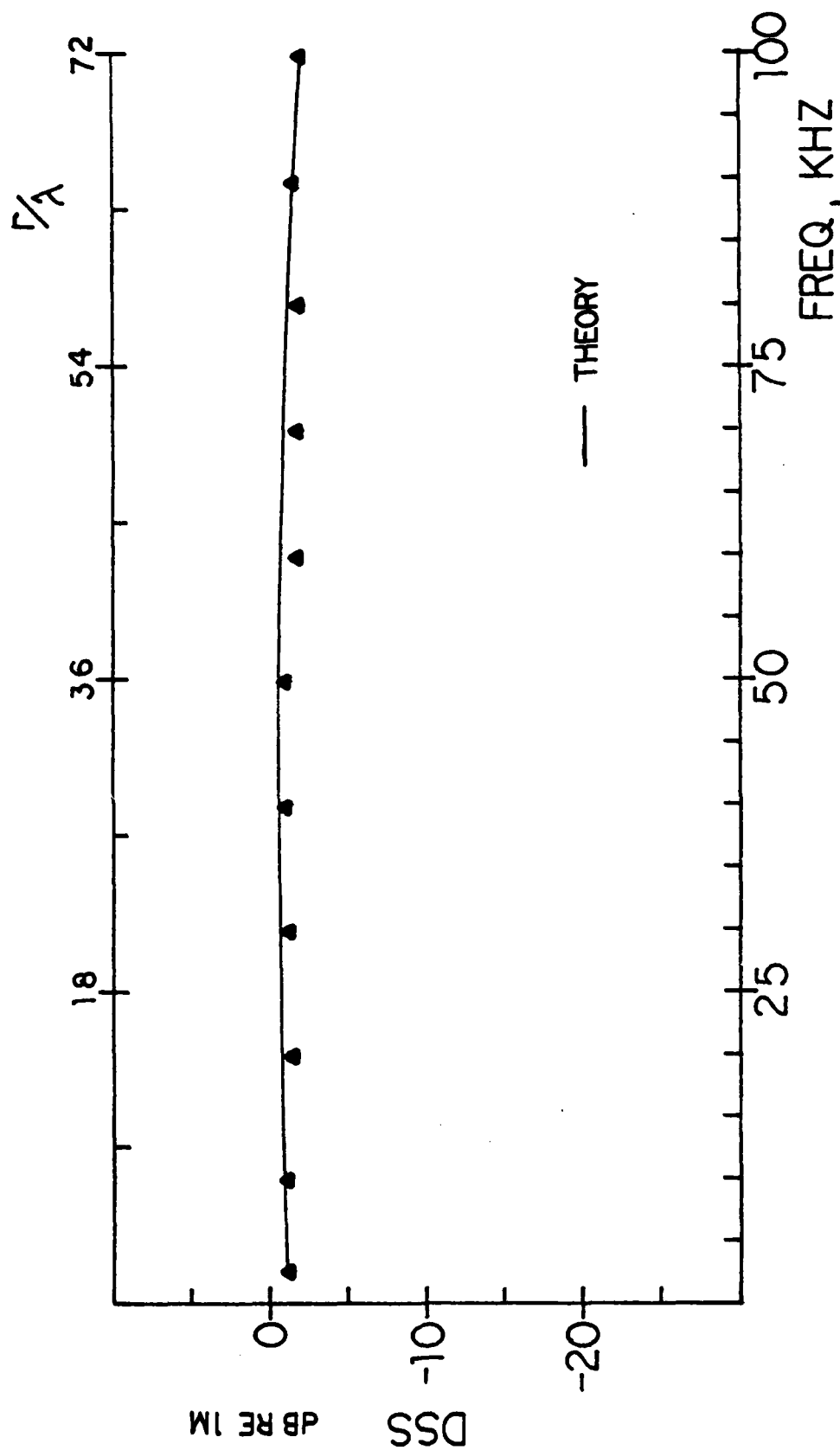


Figure 14. Diffraction scattering strength for 14° wedge;  
 $r_0 = r = 25$  cm,  $\theta_0 = 0$ ,  $\theta = \theta_w$

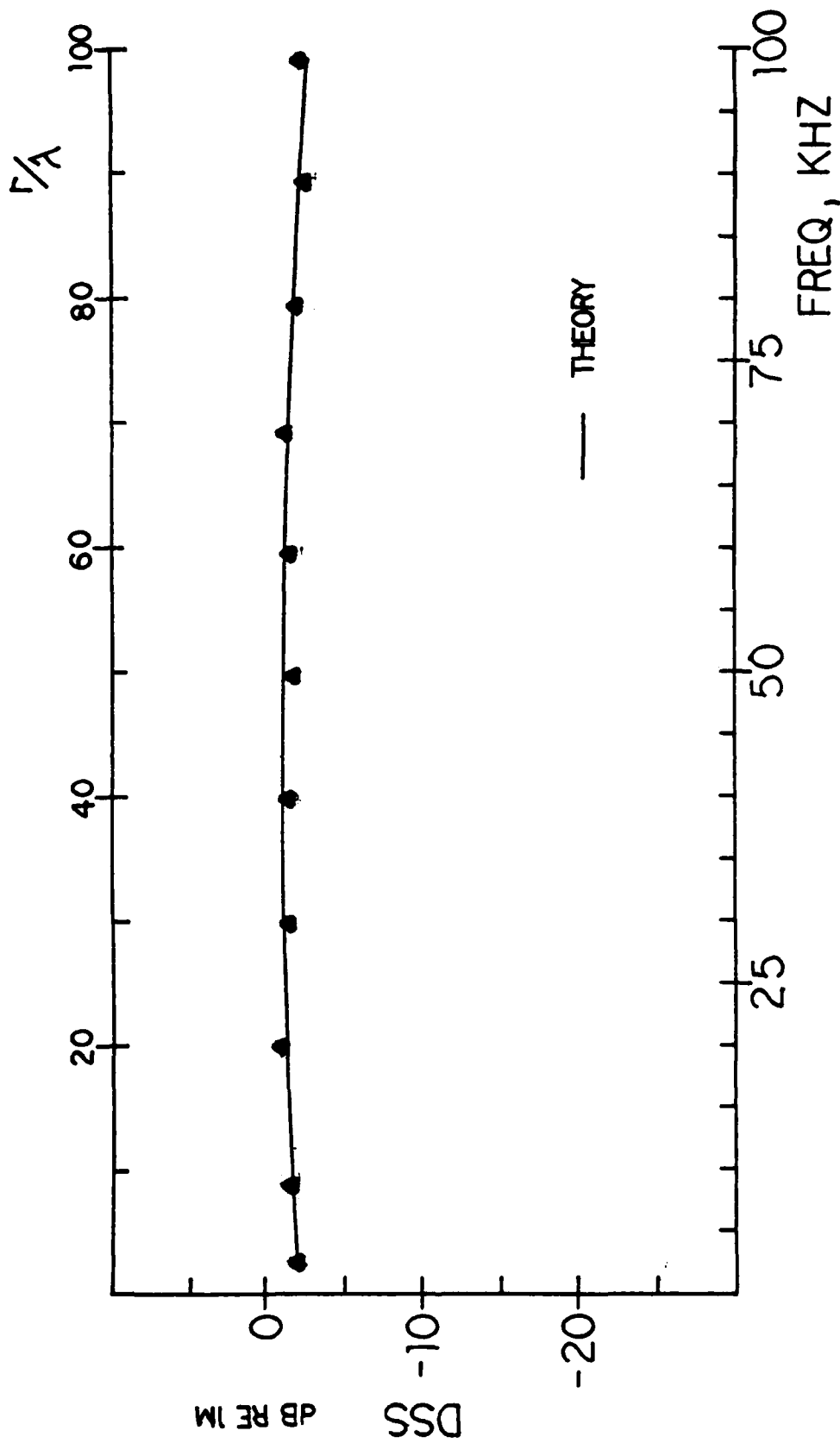


Figure 15. Diffraction scattering strength for 14° wedge;  
 $r_o = r = 35 \text{ cm}$ ,  $\theta_o = 0$ ,  $\theta = \theta_w$

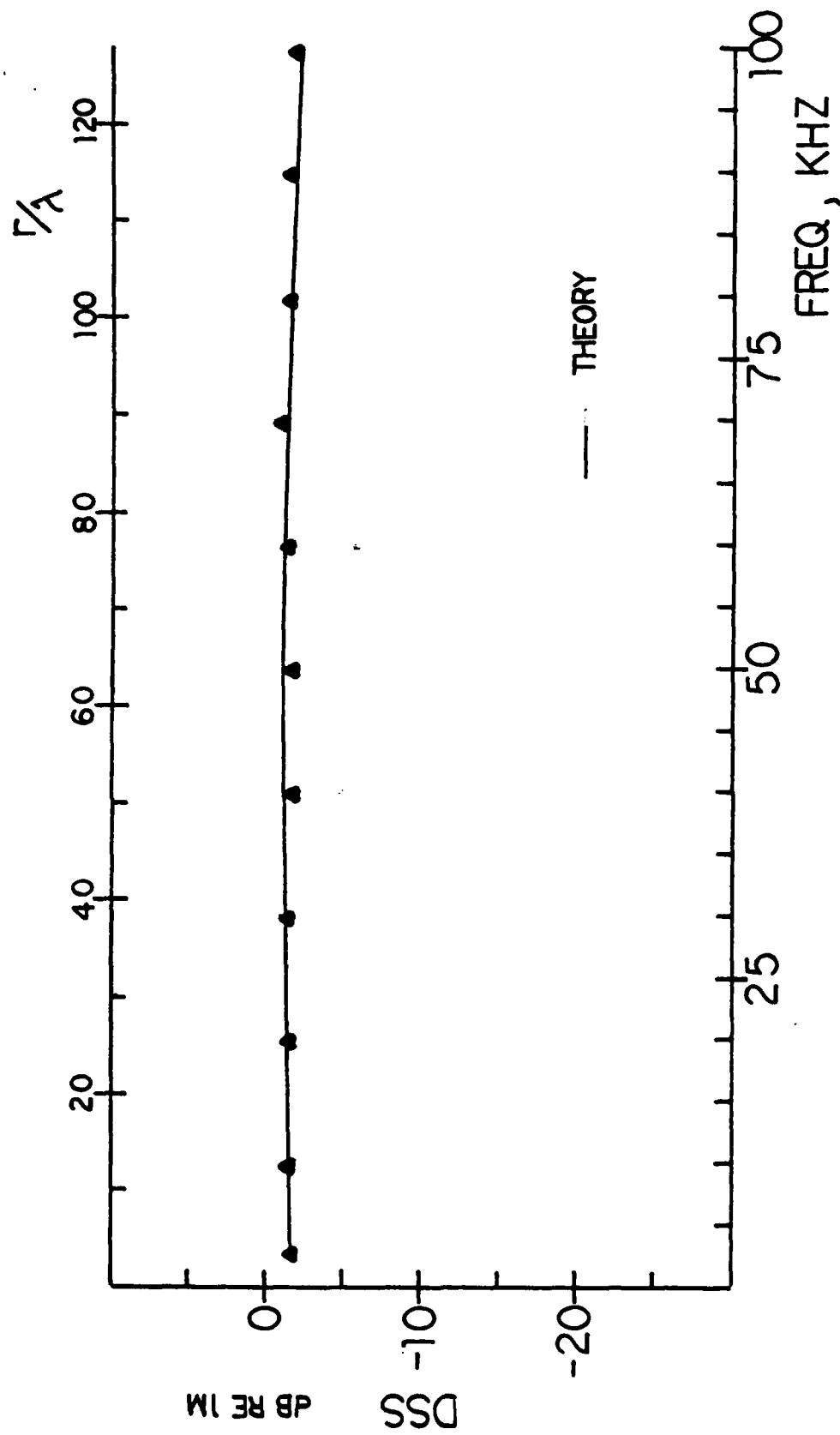


Figure 16, Diffraction scattering strength for 14° wedge;  
 $r_o = r = 45 \text{ cm}$ ,  $\theta_o = 0$ ,  $\theta = \theta_w$



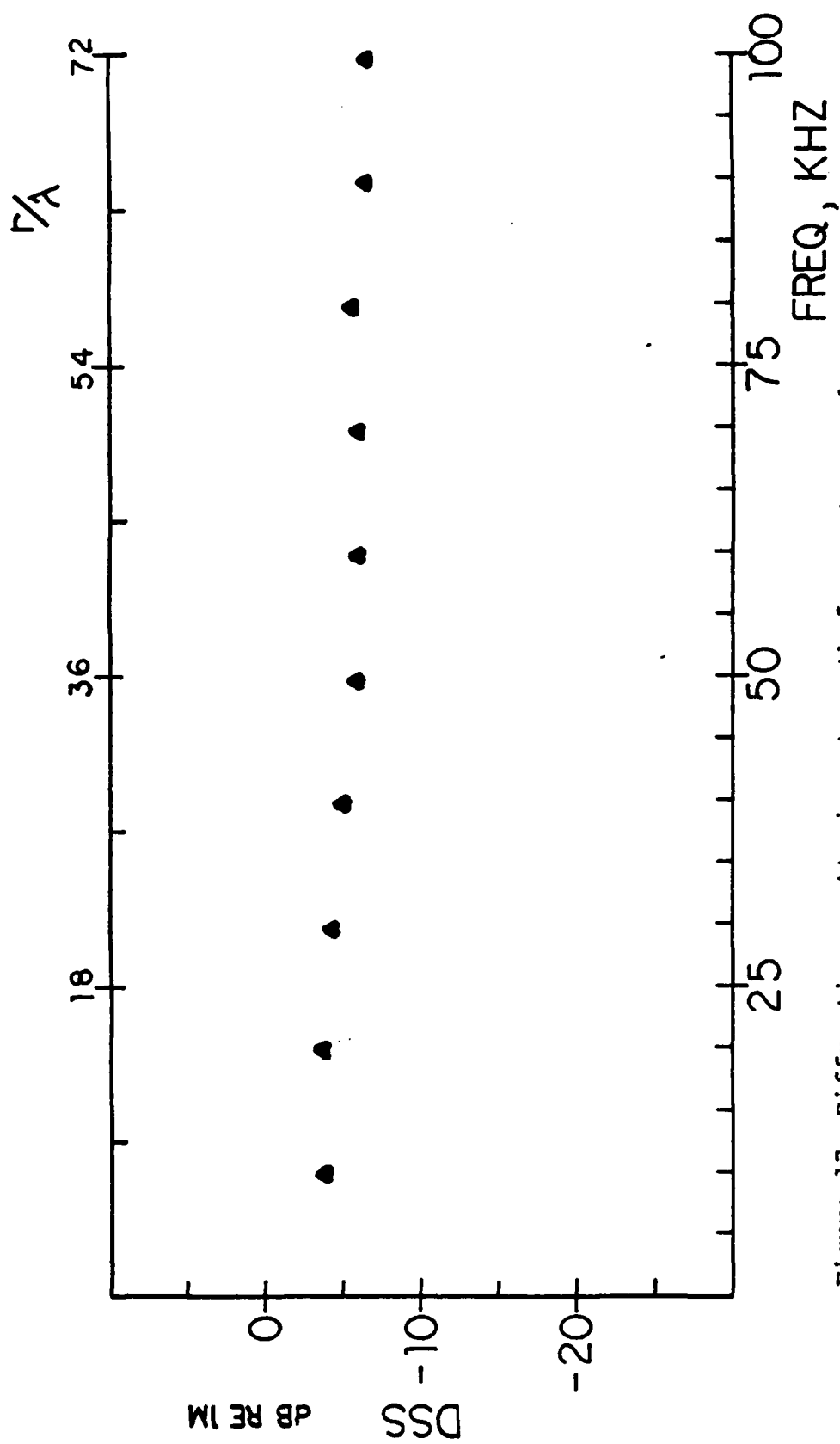


Figure 17. Diffraction scattering strength for contour wedge;  
 $r_o = r = 25$  cm,  $\theta_o = 0$ ,  $\theta = \theta_w$

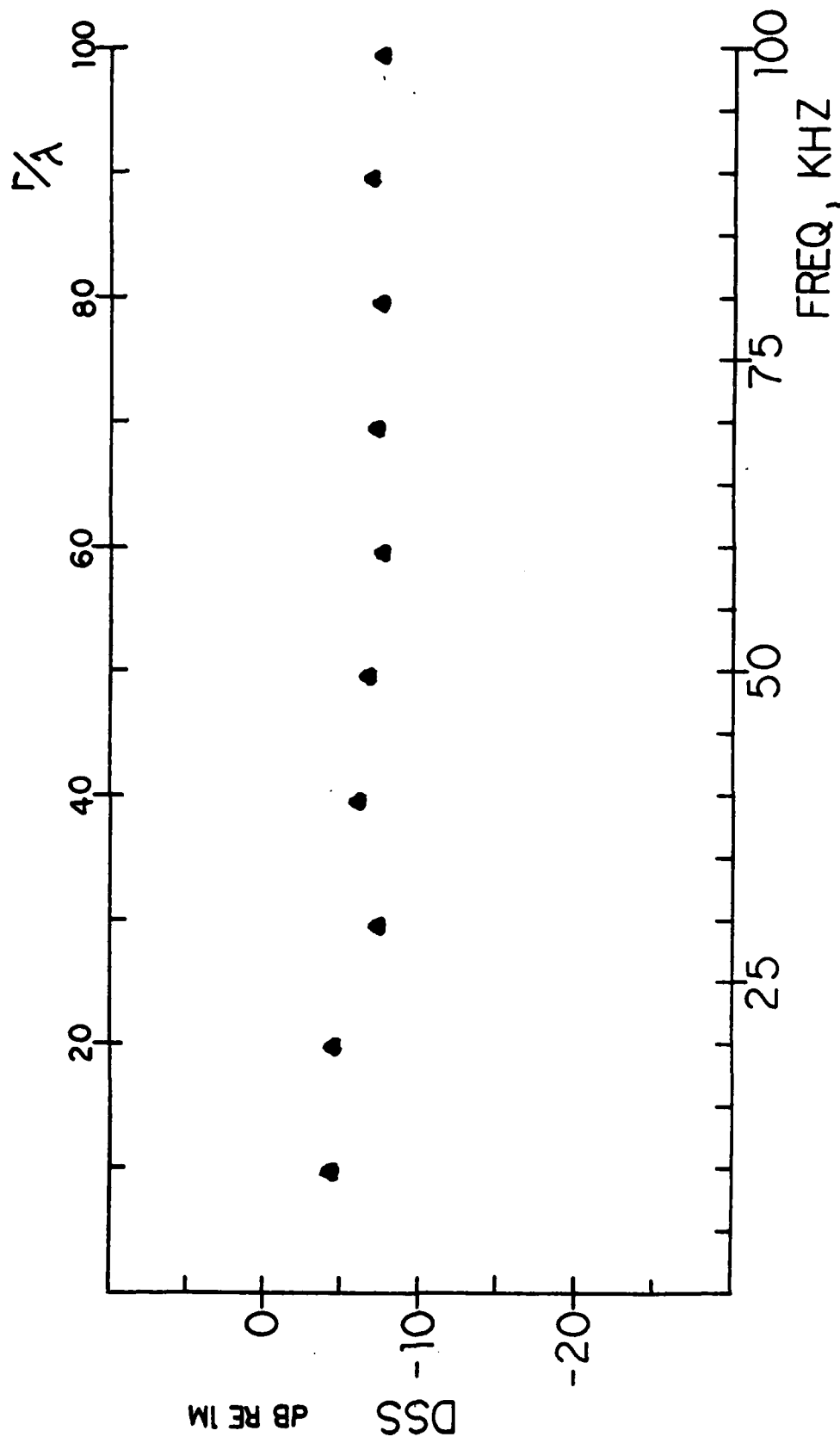


Figure 18. Diffraction scattering strength for contour wedge;

$$r_o = r = 35 \text{ cm}, \theta_o = 0, \theta = \theta_w$$

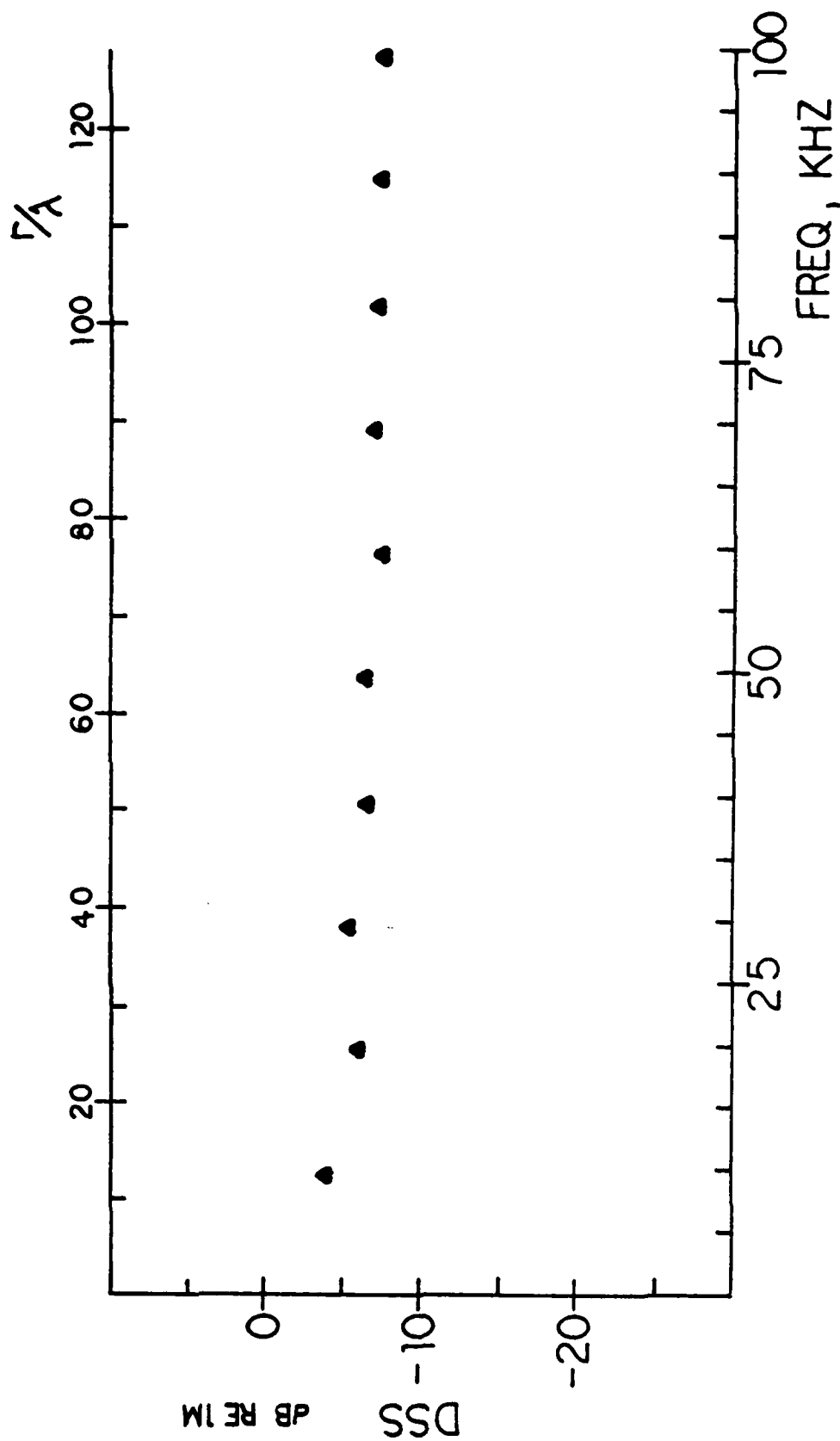


Figure 19. Diffraction scattering strength for contour wedge;

$$r_o = r = 45 \text{ cm}, \theta_o = 0, \theta = \theta_w$$

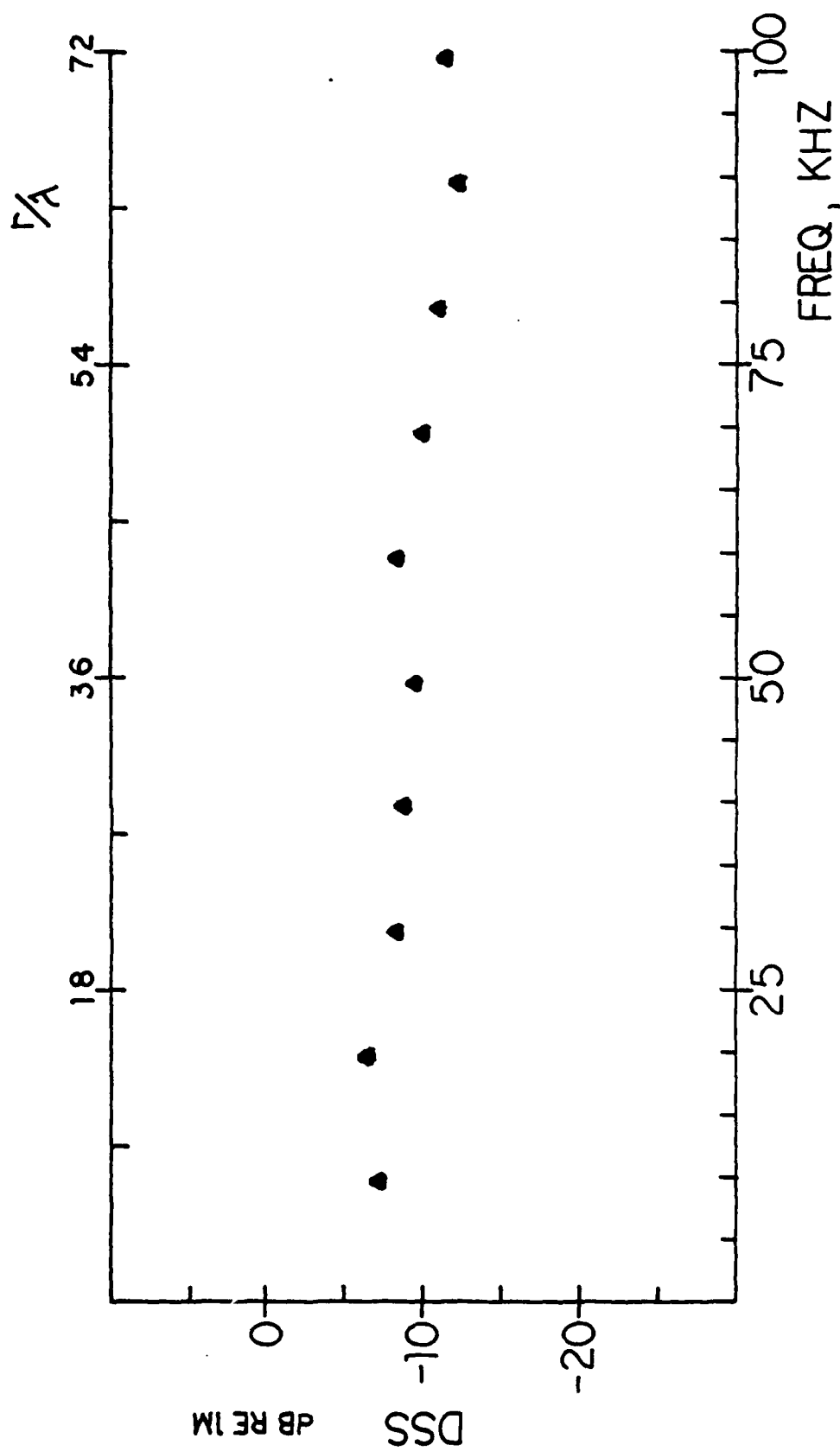


Figure 20. Diffraction scattering strength for 3D model;

$r_o = r = 25$  cm,  $\theta_o = 0$ ,  $\theta = \theta_w$

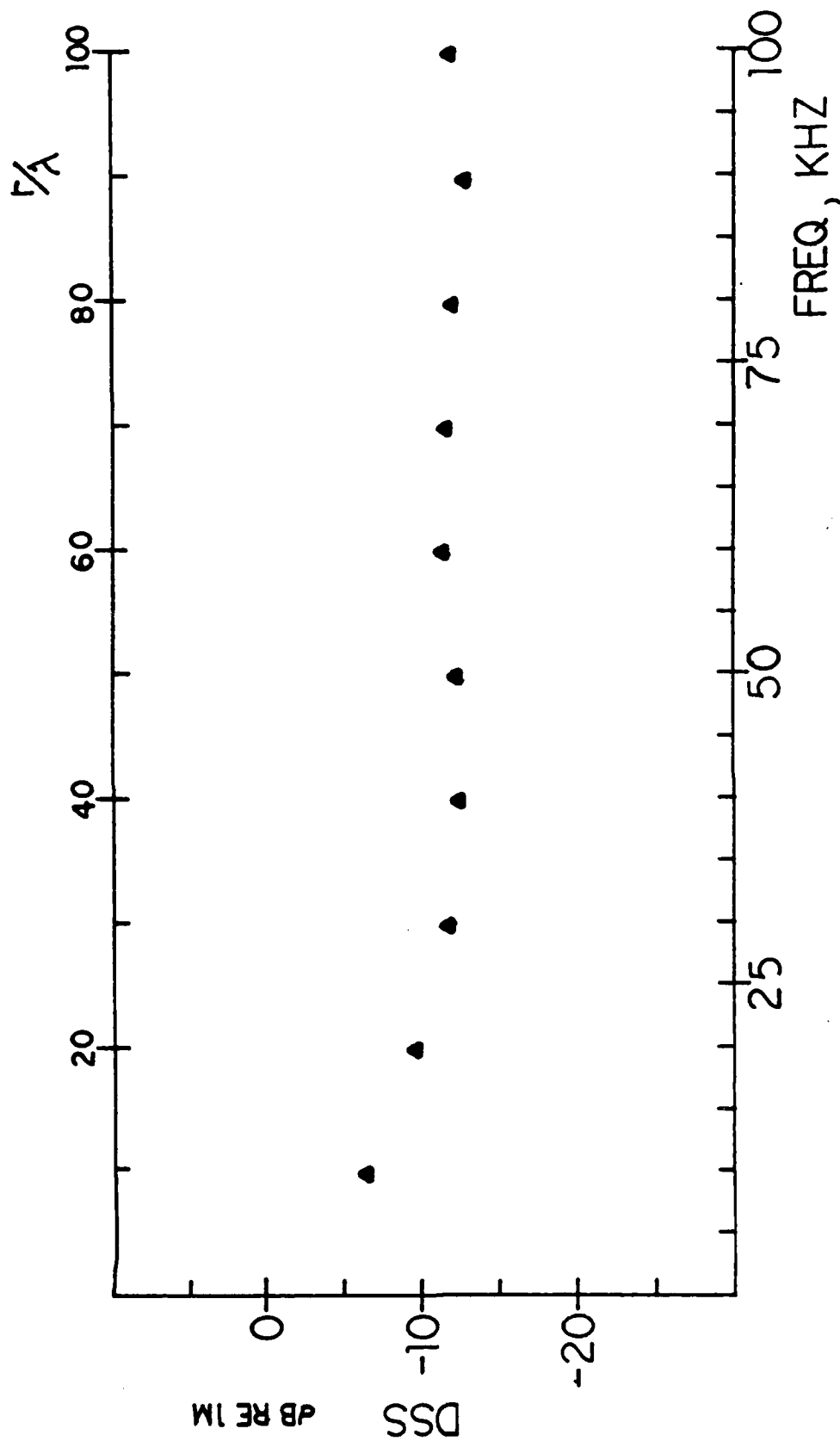


Figure 21. Diffraction scattering strength for 3D model;

$$r_o = r = 35 \text{ cm}, \theta_o = 0, \theta = \theta_w$$

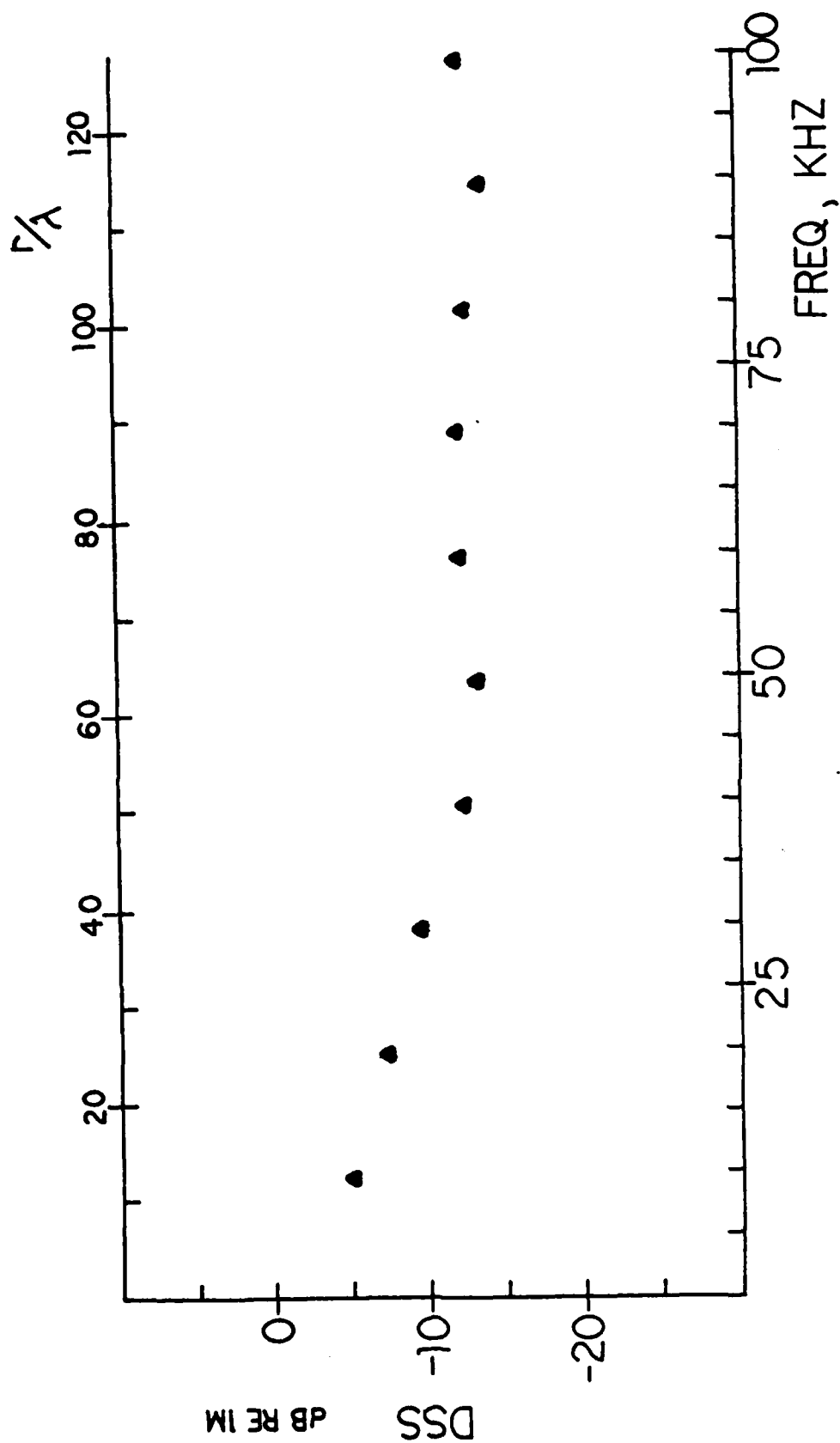


Figure 22. Diffraction scattering strength for 3D model;

$$r_o = r = 45 \text{ cm}, \theta_o = 0, \theta = \theta_w$$

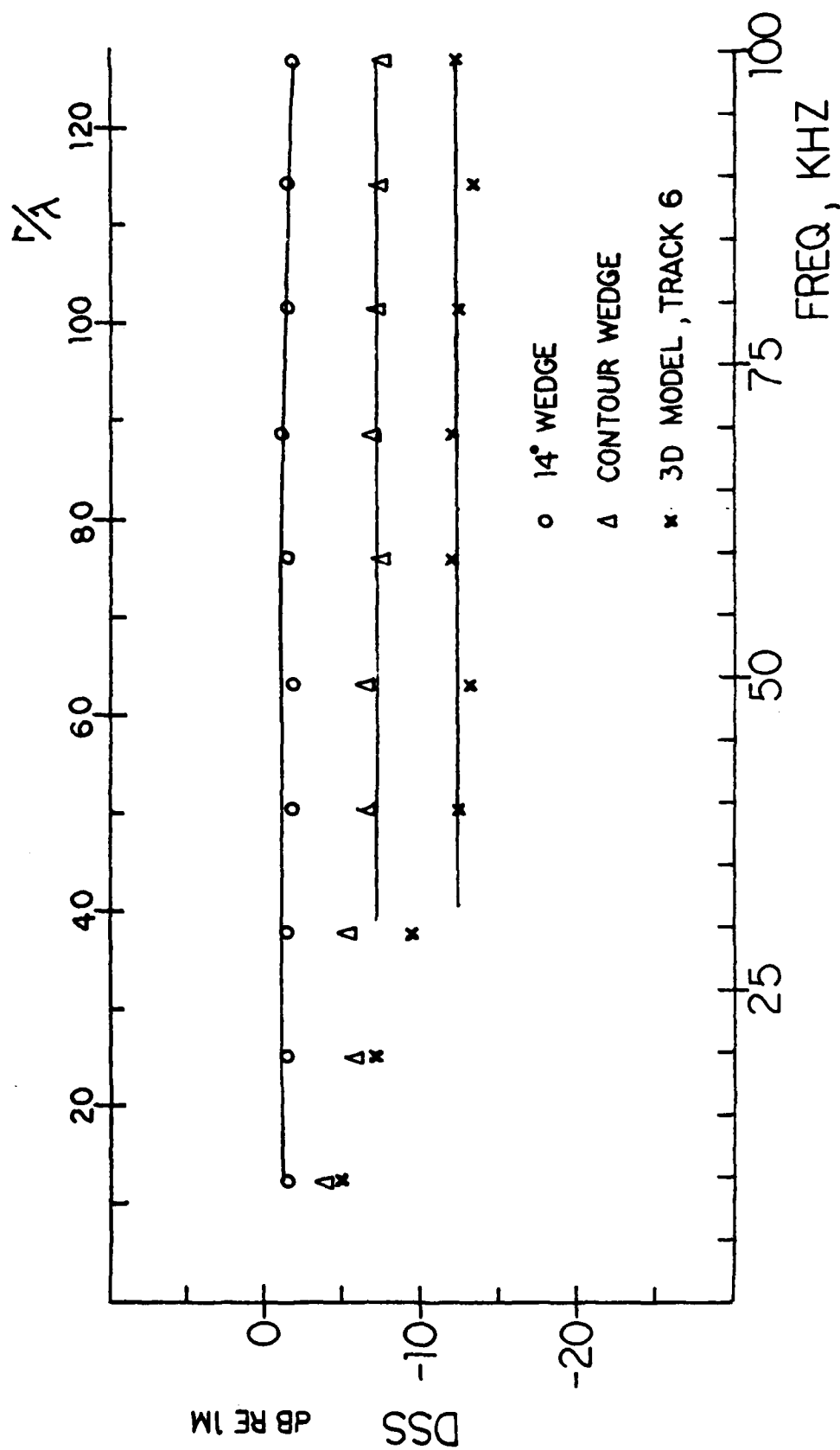


Figure 23. Comparison of diffraction scattering strength by model;

$r_o = r = 45 \text{ cm}$ ,  $\theta_o = 0$ ,  $\theta = \theta_w$ . Solid lines represent theory for 14° wedge and asymptotes for contour wedge and 3D model.

-1 dB throughout the range of frequencies studied. This may be attributed to the fact that only the single, sharp crest of the simple wedge is doing all the diffracting for all frequencies. The  $f^{\frac{1}{2}}$  behavior of the Biot-Tolstoy theory is effectively absorbed by the definition of DSS. There are no other variations along the sound travel path for the wavefronts to interact with.

Sound propagating over the contour wedge, however, is confronted both with a rounded rather than sharp crest and with a gently undulating surface rather than a plane surface. The variations introduce secondary scatter thereby lowering the DSS. Nevertheless an asymptotic value is reached for  $r/\lambda > 50$ .

The 3D model, with a much more irregular surface, offers additional secondary scattering effects. Again, the secondary scatter is frequency dependent; as the wavelength becomes comparable to or smaller than the various dips and bumps in the contour, secondary scatter takes place. At  $r/\lambda \leq 10$  secondary scatter is at a minimum and the DSS of all models approach the same value. The frequency dependent behavior is clearly evident for  $10 \leq r/\lambda \leq 50$ . At  $r/\lambda > 50$  there is again an asymptotic, far-field, value, although it is lower than for either of the simpler models.

These results clearly show that the experimental study of diffraction by complex barriers, and particularly any attempt to duplicate or predict real-world data, requires a



three dimensional (3D) model. The remainder of this work will be based on data taken from the 3D model of Dickens Seamount.

### C. ACOUSTICAL SURVEY OF THE 3D MODEL

To further understand the variability in diffracted acoustic energy by the 3D model, an acoustical survey was performed.

#### 1. Sensitivity To Contour

The sensitivity to contour along the sound travel path (track 6) was investigated by varying  $r_0$  and  $r$  to successively greater symmetrical distances from the crest. The angles of the source and receiver were kept at  $\theta_s = 0$ ,  $\theta_r = \theta_w$ . Figure 24 illustrates the results. As  $r_0$  and  $r$  are moved, the falloff of the DSS is different as more of the model contour is acoustically exposed thereby activating more secondary scatter points. At  $r/\lambda > 50$ , the three curves fair into the same asymptote, DSS = -12 dB.

These data also show that the DSS is approximately constant at a given  $r/\lambda$  regardless of whether  $r$  or  $\lambda$  is varied.

Looking at  $r/\lambda \leq 50$  there is evidence that the diffracted energy reaching the microphone is a summation from the various radiation points with some degree of coherence. In the case studies, an average curve could be given such that the secondary scatterers result in a variation of  $\pm 2$  dB around the average for  $r/\lambda < 50$ .

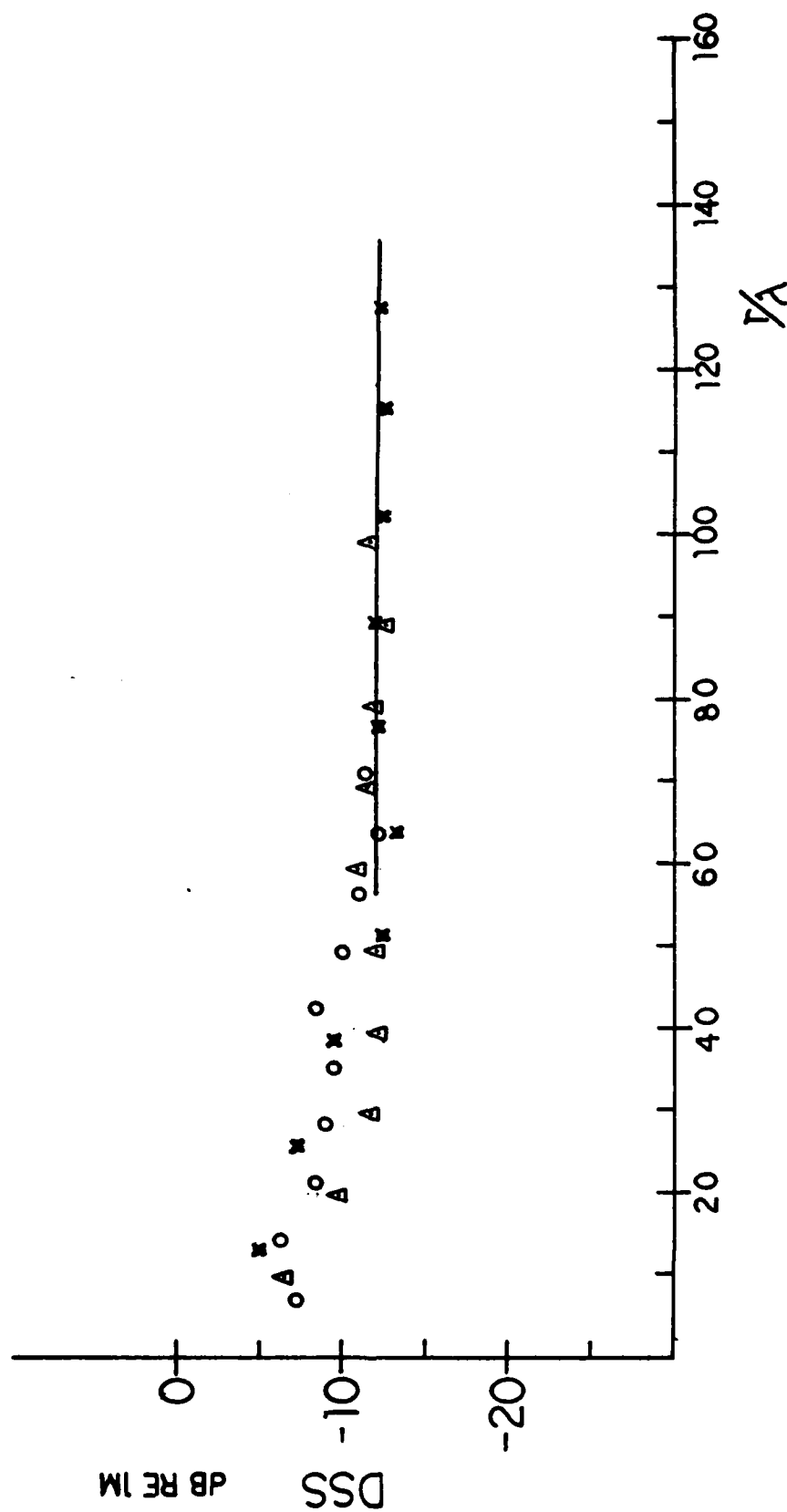


Figure 24. Comparison of diffraction scattering strength as a function of source/receiver range from crest;  
 $\theta_o = 0, \theta = \theta_w$ .

## 2. Sensitivity To Position Of Ridge Crossing

The sensitivity to the position of ridge crossing was investigated by transmitting sound over the model at various paths roughly perpendicular to the ridge line. Figure 8 depicts the path locations on the seamount. The source/receiver distance was kept constant at 45 cm (3.54 km) and  $\theta_o = 0$ ,  $\theta = \theta_w$ ; i.e., source and receiver on the surface. Figures 25 through 30 illustrate the separate results. Figure 31 is a composite of the experimental curves. Figure 32 gives a comparison of contours along each path. Note that there is no great change in  $w$  and consequently there is little difference in DSS at  $\frac{r}{\lambda} = 10$  for the various paths. At higher frequencies, however, the distinct contours each have their own secondary scatter characteristics and the different DSS curves reflect this.

Figure 25 warrants some additional comment. As can be seen, the DSS curve is atypical compared with other data. The 3D model undergoes some radical changes in topography close to path 1 (See Figure 8). To one side of the path there is a rapid falloff in elevation. It is believed that this extreme change in contour is responsible for interfering secondary scatter, accounting for the variability in DSS when it should be asymptotic.

It also should be noted that for the duration of the data taking for this section, there was a noticeable increase in electronic interference within the building resulting, in particular, in great variability of the 88 kHz data point.

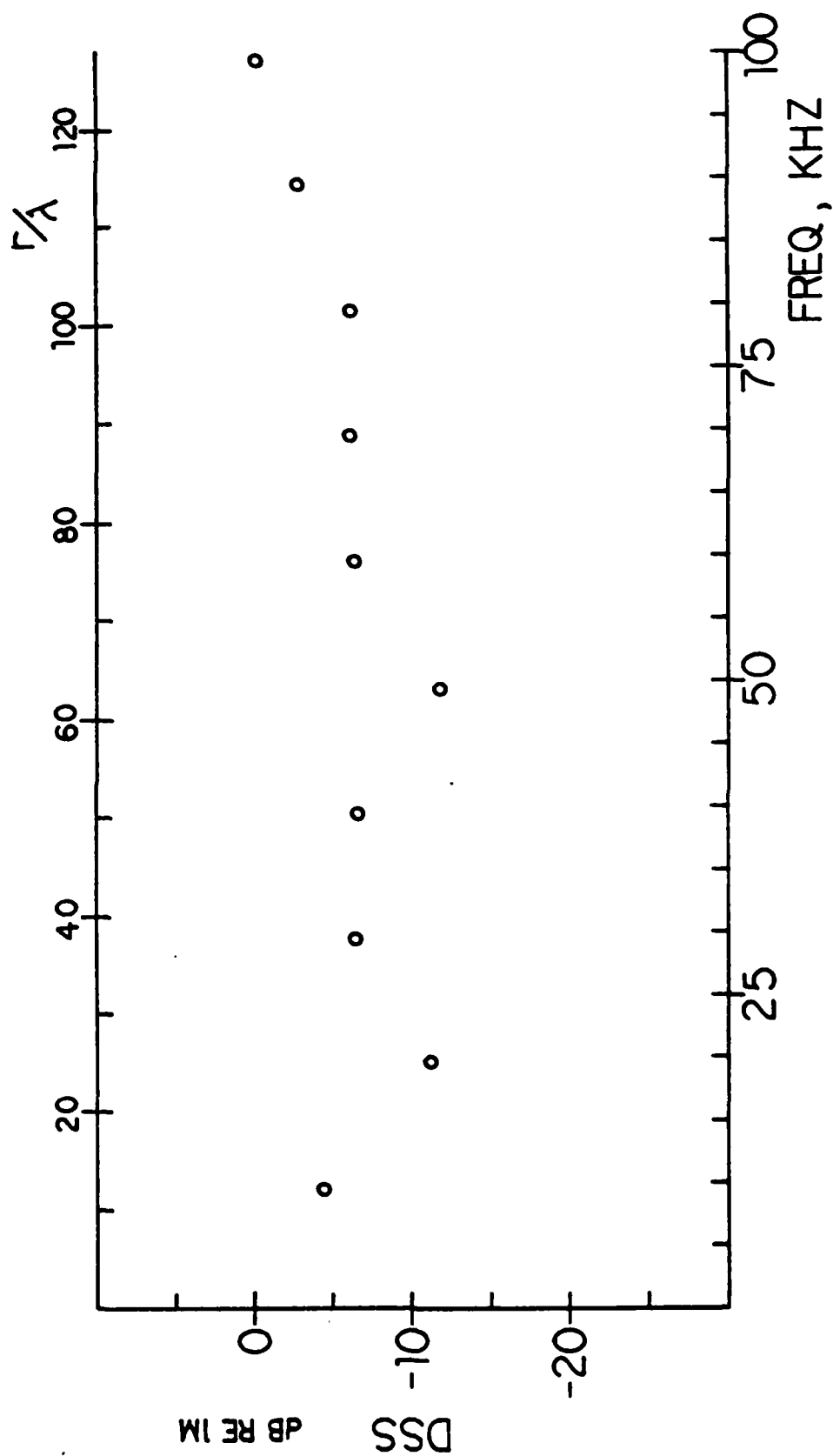


Figure 25. Diffraction scattering strength for 3D model, path 1;

$r_0 = r = 45$  cm (3.54 km),  $\theta_0 = 0$ ,  $\theta = \theta_w$ .

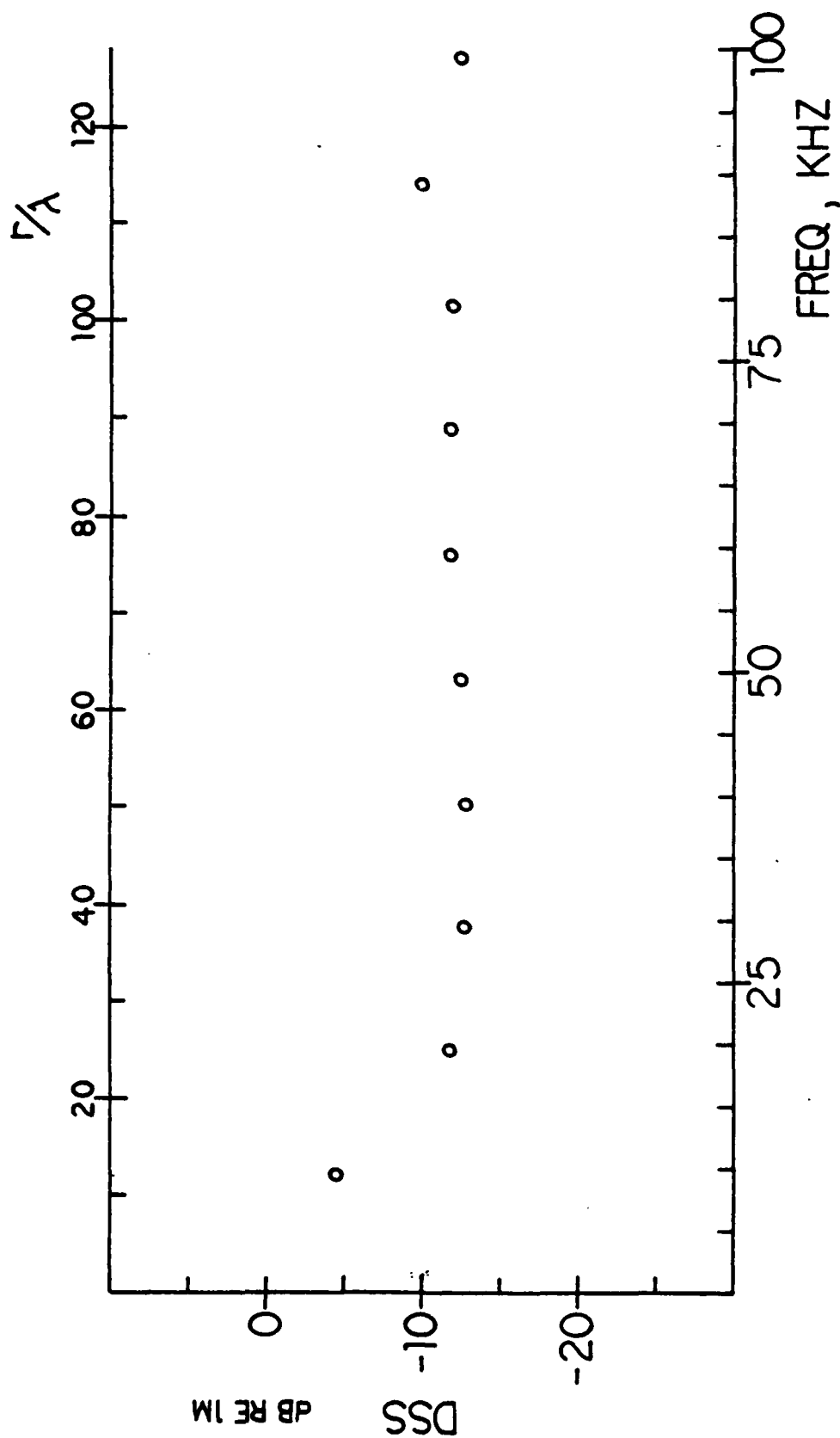


Figure 26. Diffraction scattering strength for 3D model, path 2;

$r_o = r = 45$  cm (3.54 km),  $\theta_o = 0$ ,  $\theta = \theta_w$ .

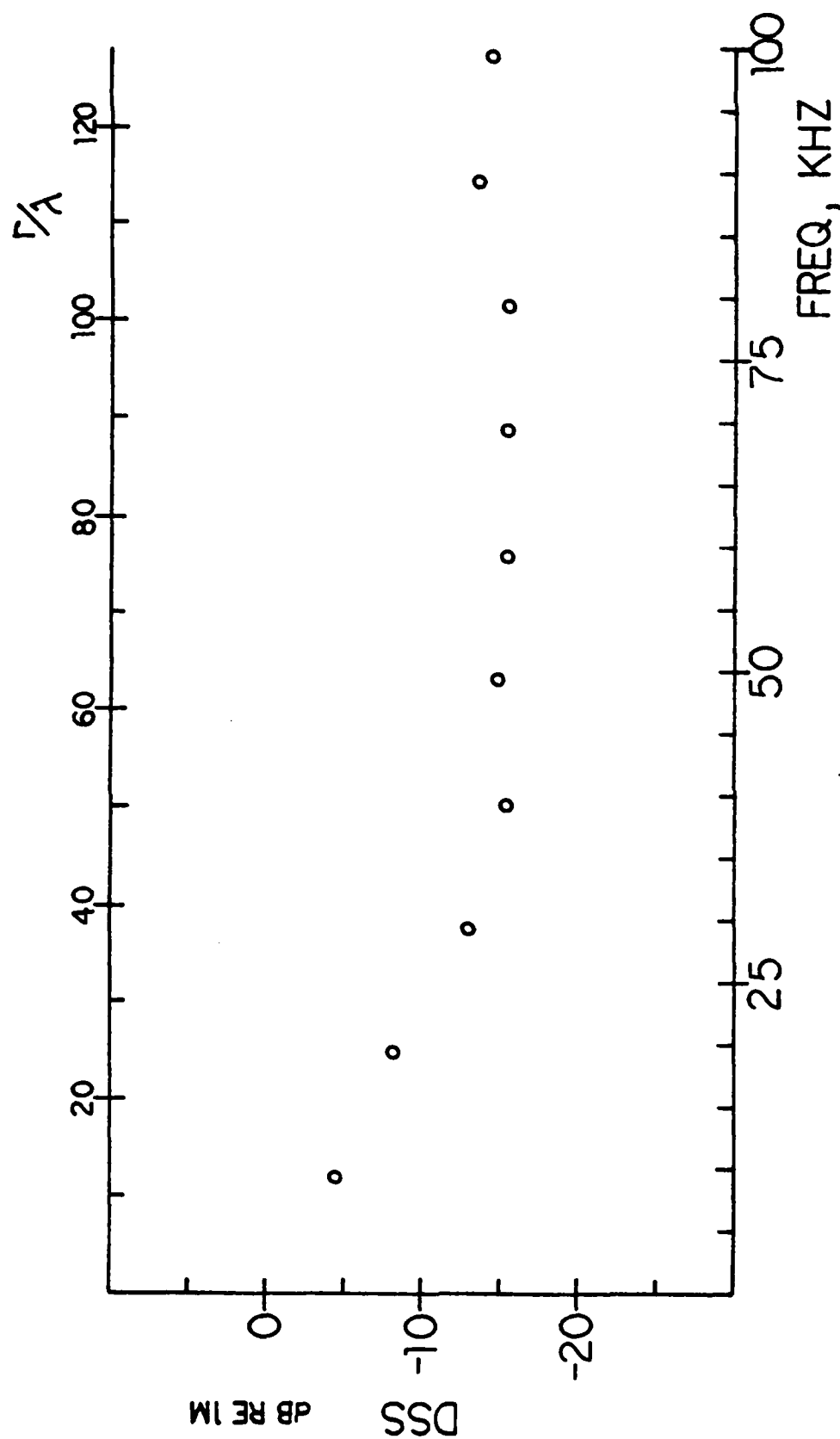


Figure 27. Diffraction scattering strength for 3D model, path 3;  
 $r_o = r = 45$  cm (3.54 km),  $\theta_o = 0$ ,  $\theta = \theta_w$ .

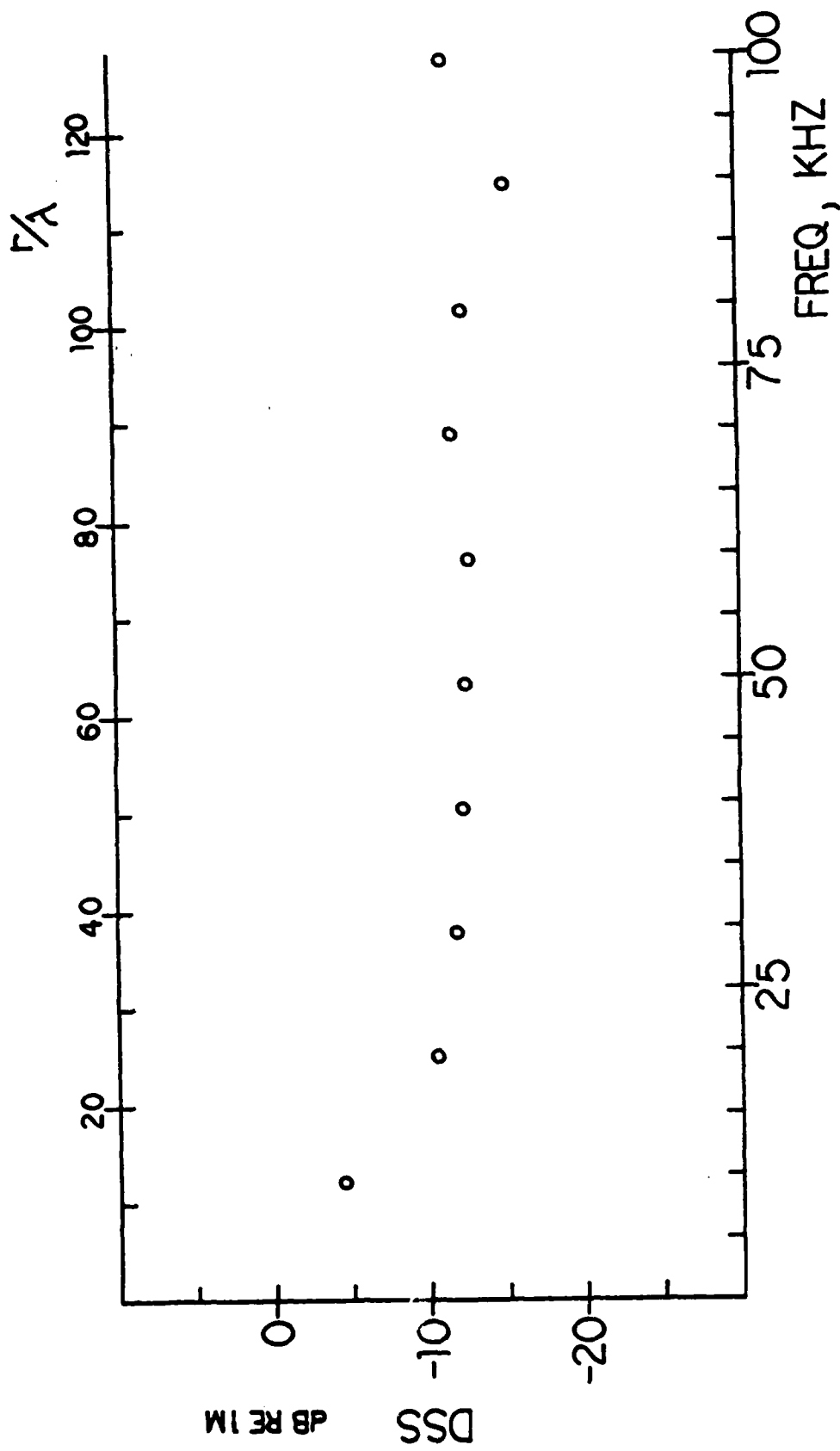


Figure 28. Diffraction scattering strength for 3D model, path 4;  
 $r_o = r = 45$  cm (3.54 km),  $\theta_o = 0$ ,  $\theta = \theta_w$ .

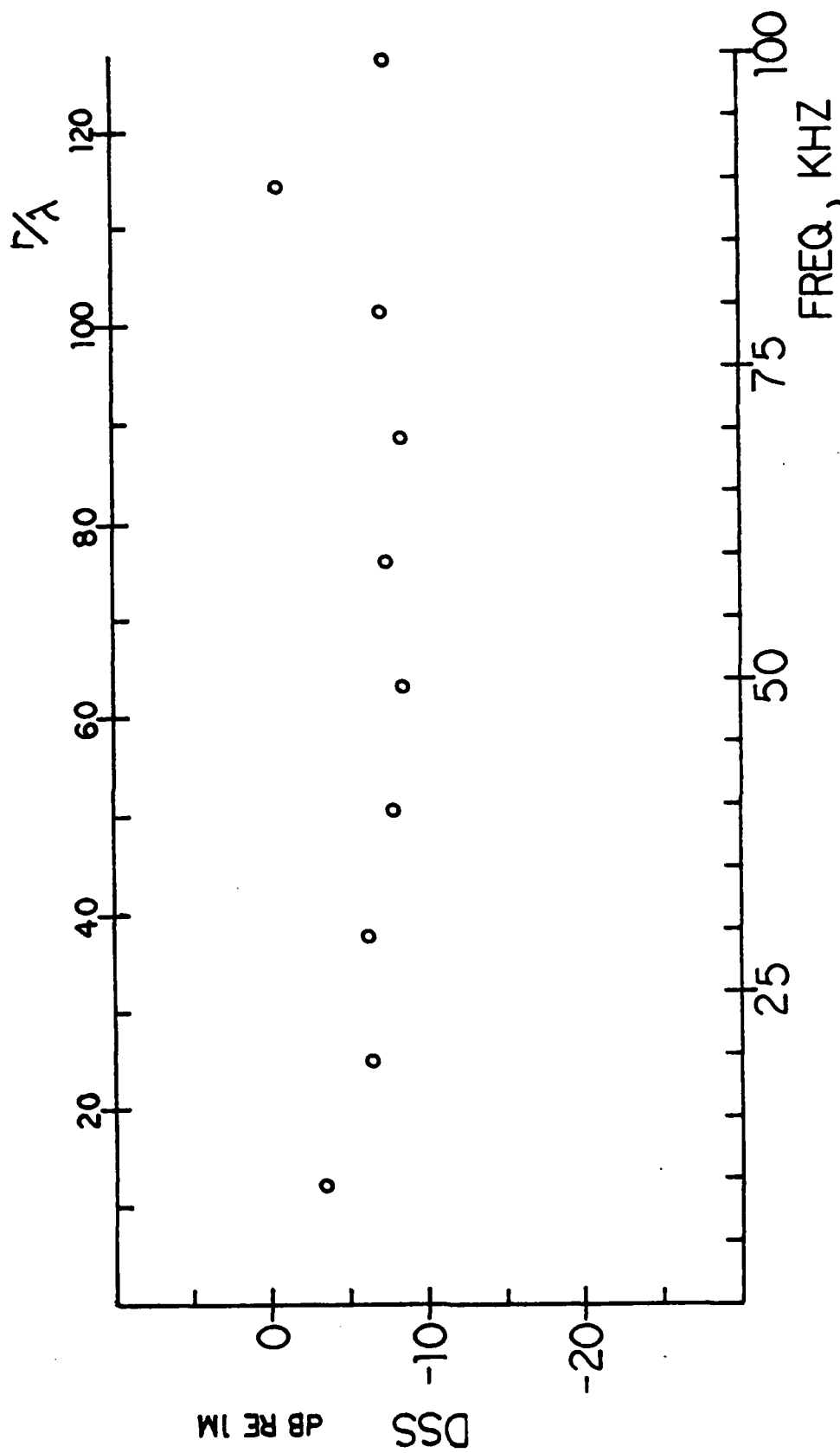


Figure 29. Diffraction scattering strength for 3D model, path 5;  
 $r_o = r = 45$  cm (3.54 km),  $\theta_o = 0$ ,  $\theta = \theta_w$ .



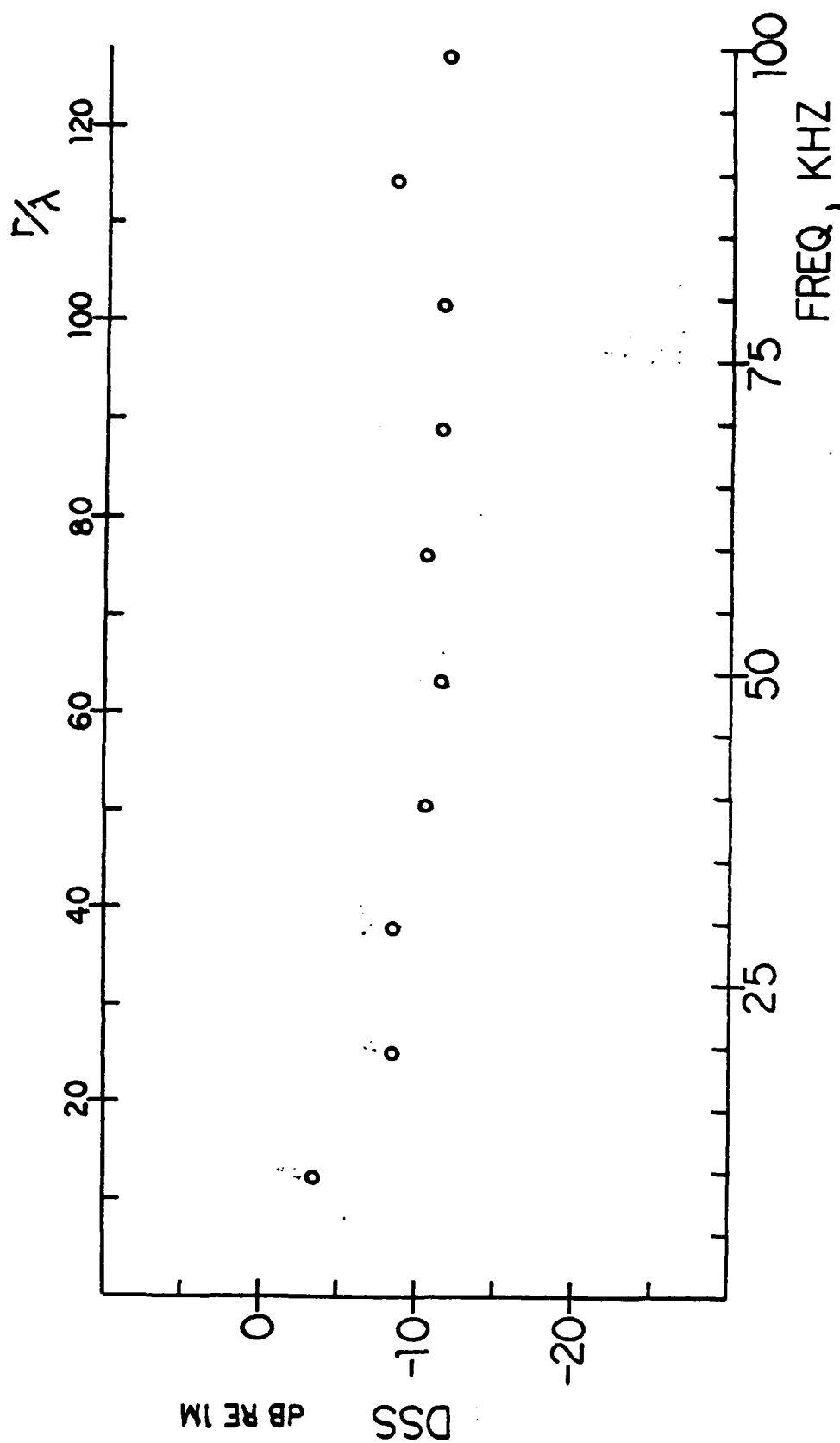


Figure 30. Diffraction scattering strength for 3D model, path 6;

$r_o = r = 45$  cm (3.54 km),  $\theta_o = 0$ ,  $\theta = \theta_w$ .

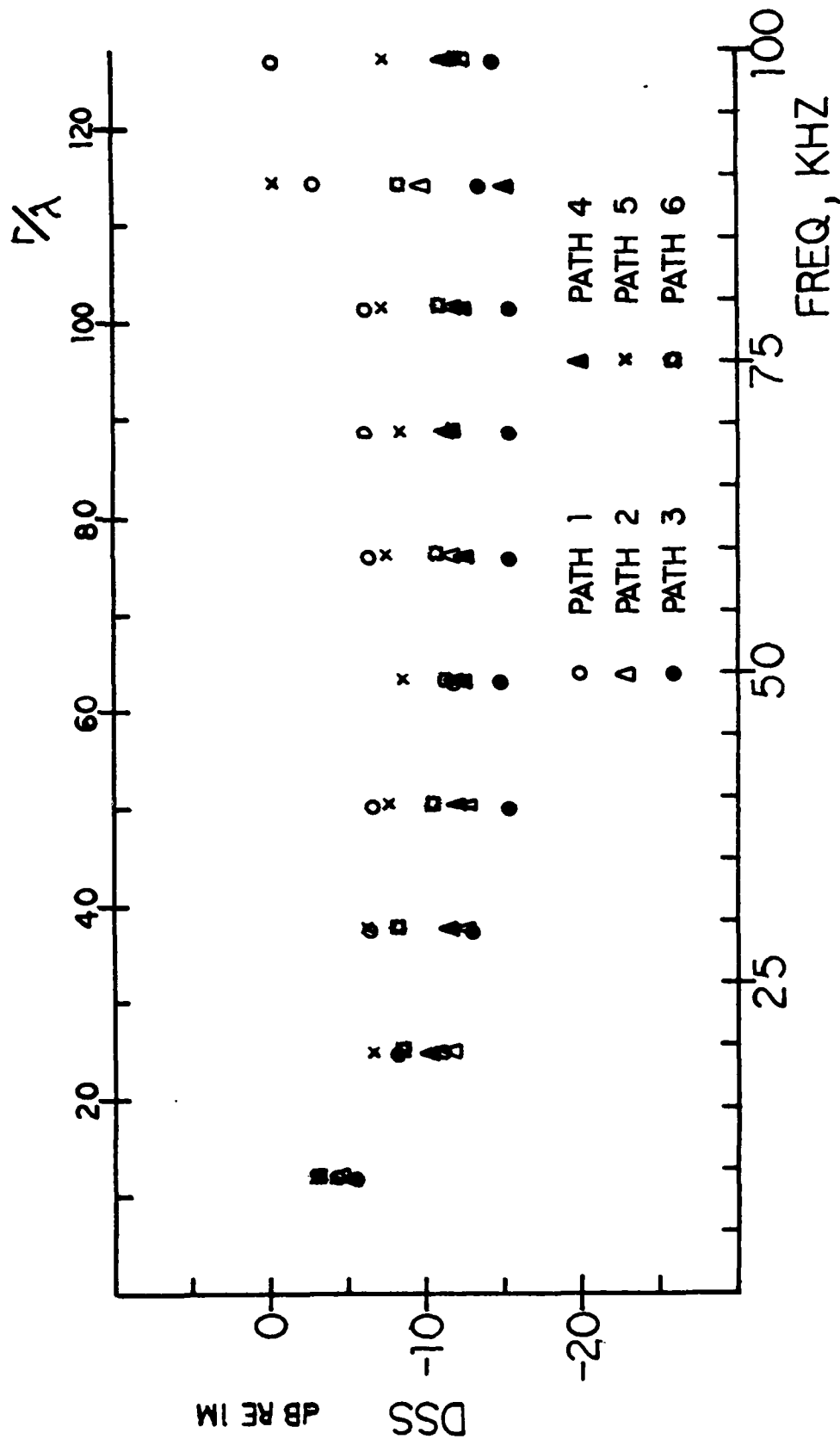
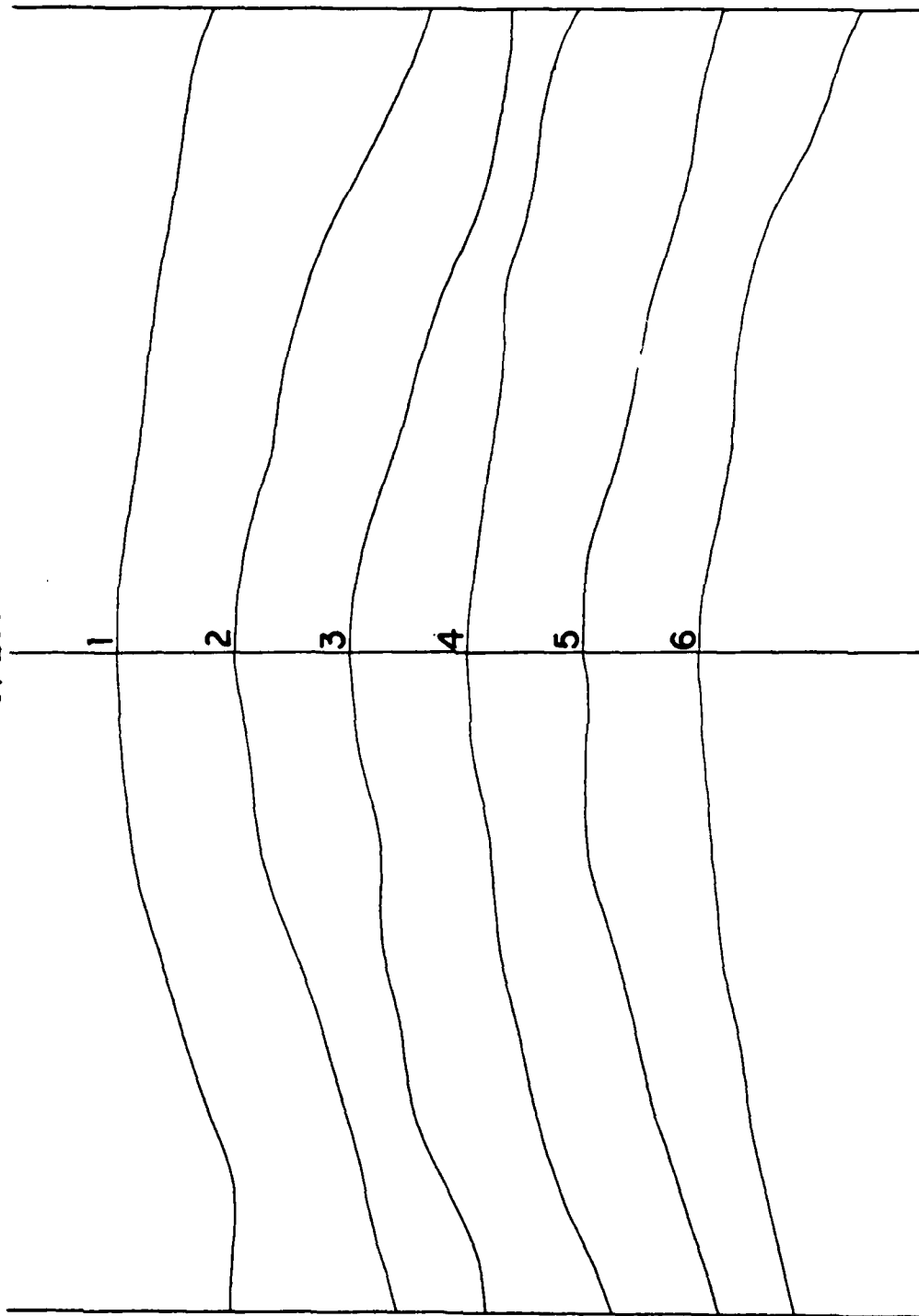


Figure 31. Diffraction scattering strength for 3D model as a function of path;  $r_o = r = 45$  cm (3.54 km),  $\theta_o = 0, \theta = \theta_w$ .

**R = 45CM**

**R = 45CM**



**Figure 32. Comparison of contour along paths 1 through 6**

### 3. Sensitivity To Sample Window Duration

The DSS also has a dependence on how much of the model has been acoustically exposed during the opening of the sampling window. To investigate this sensitivity, three sampling window durations were used: 102, 204, and 410  $\mu$ s. These corresponded to receiving energy being reradiated by the ridge of the seamount, at distances 11.2 cm (882 m), 16.1 cm (1.76 km), and 23.5 cm (3.53 km, respectively, measured on both sides of the least time travel path. In theory, as the sampling window is extended, the DSS should increase to a maximum value and then remain constant. This is due to relatively constant reradiation of energy from the wedge crest out to approximately 20 cm (1.6 km) from the least time travel path or  $z = 0$  [Ref. 27]. Beyond that, the falloff of reradiated energy is rapid and the contribution to the diffracted pulse is negligible.

Figure 33 illustrates the results of this investigation of the 3D model. As can be seen, when the sampling window is extended from 102 to 204  $\mu$ s, the DSS at the higher frequencies decreases. It is surmised that partial destructive interference is taking place at the greater window openings. However, the difference in DSS using the 204 and 410  $\mu$ s sampling window is only about 1 dB, suggesting that at the larger openings the interference has reached its maximum and that contributions from the greater ridge distance as predicted are no longer significant.

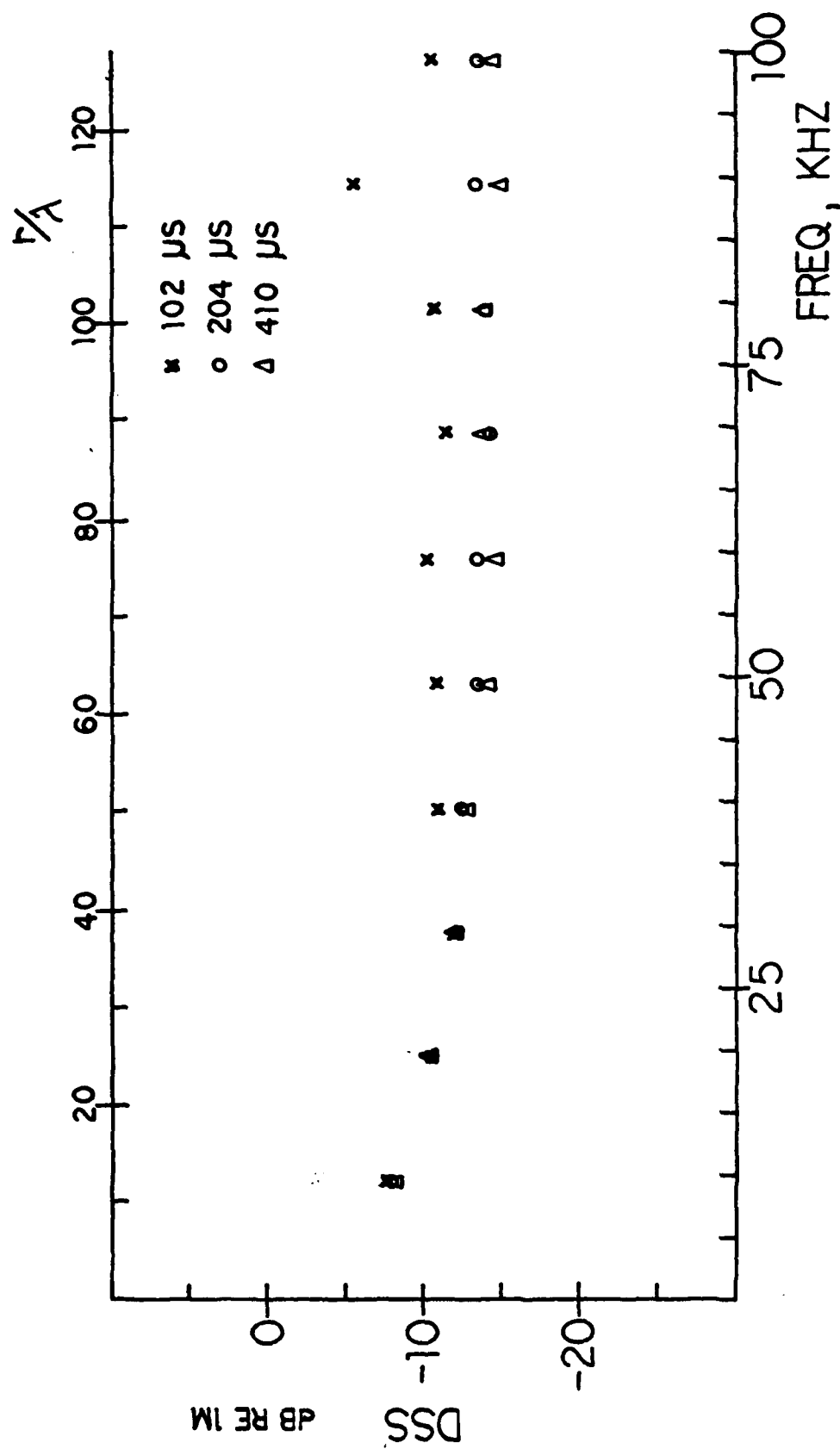


Figure 33. Diffraction scattering strength for 3D model as a function of sampling window duration;  $r_o = r = 45$  cm ( $3.54$  km),  $\theta_o = 0$ ,  $\theta = \theta_w$ .

#### 4. Sensitivity To Azimuth

To investigate the sensitivity to the angle of ridge crossing, or azimuth, the source was set at  $r_0 = 45$  cm,  $\theta_0 = 0$ , and  $z_0 = 0$  with the least time travel path in the center of the model. The receiver was positioned at  $r = 45$  cm,  $\theta = \theta_w$ , but  $z$  was varied from  $z = 0$  to  $z = \pm 25$  cm,  $\pm 50$  cm. These distances corresponded to  $\pm 2$  km and  $\pm 4$  km at Dickens. Figure 34 illustrates the results. At angles off from the least time path the diffraction loss is greater.

#### D. COMPARISON OF LABORATORY PREDICTIONS WITH AT-SEA DATA

The total propagation loss measured at Dickens for the case where all the rays from the sound source are blocked by the seamount is approximately +100 dB re 1M (Case A, Fig. 5). It is postulated that this propagation loss is composed of four distinct components: (1) the propagation loss (spreading and refraction loss) from the source to the side of the seamount, (2) a forward scattering loss when the wavefronts impinge upon the seamount surface and propagate toward the crest, (3) diffraction loss going over the seamount, and (4) the propagation loss from the crest of the seamount to the receiver. If these separate propagation losses can be determined analytically or experimentally then, if the diffraction description is correct, their summation should approach what was actually measured at sea.

The prediction therefore combines two approaches: ray theory to describe the frequency independent refraction from

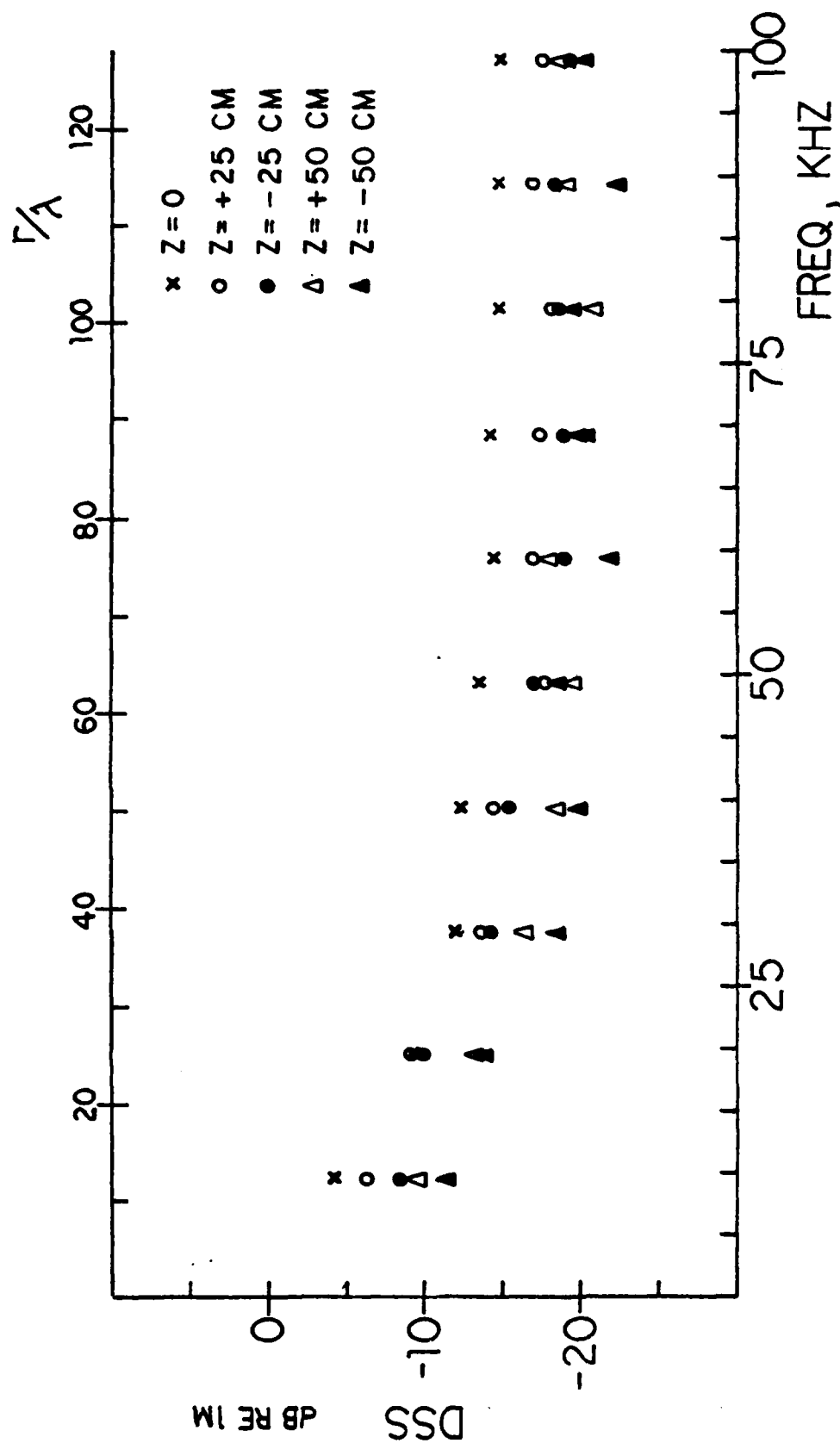


Figure 34. Diffraction scattering strength for 3D model as a function of  $z$ ;  $r_o = r = 45$  cm (3.54 km),  $\theta_o = 0$ ,  $\theta = \theta_w$ .

source to seamount to receiver, and physical modeling based on wave theory to describe the frequency dependent propagation over the seamount. For this work the propagation losses due to refraction and divergence were determined by computer at the Naval Postgraduate School utilizing FACT models which were parts of the Integrated Command ASW Prediction System (ICAPS). The forward scattering and diffraction losses at the seamount were determined experimentally using the 3D model.

#### 1. Measurement Of Scattering Loss

As the wavefronts emanating from the source contact the surface, forward scatter takes place which directs energy upslope to the crest and parallel to the surface. Theories are available for the prediction of forward scatter from a statistically rough plane surface. However, no information about the surface roughness at Dickens is available. Furthermore, the topographical roughness of the upslope of Dickens along track 6 is what is specifically needed. Therefore, an experimental measurement of the topographical forward scatter was performed. The objective was to compare scattered acoustic energy near the crest with incident energy upon the surface.

The low Q sound source used for the particular experiment was a 8 by 9 cm rectangular solid dielectric transducer. The measured radiation patterns for 50 and 100 kHz are shown in Figure 35. The receiver was a 1/2" B&K microphone because its size was small enough to collect scattered radiation at the surface.



Referring to Figure 5 it can be seen that the middle of the cone of incoming rays from the source corresponds closely with the midpoint of the upslope. Consequently, this was chosen as the aim point for the maximum response axis of the source. The receiver was placed at a position on the upslope corresponding to the intercept point of the uppermost rays. The geometry of the experiment is illustrated in Figure 36.

The transient signal utilized was a single cycle of a 50 kHz and then a 100 kHz sine wave. The results are given in Figures 37 and 38. The first oscillation is the direct path signal; this is followed by 3 or 4 cycles of receiver ringing. The arrival of the major portion of the scattered radiation is indicated by the large amplitude oscillations at approximately 120  $\mu$ s following the direct path arrival.

To estimate the decibel measure of the scattering loss the ratio of the voltage amplitude of the two signals is used. For both the 50 and 100 kHz cases the scattered signal is approximately double the direct path signal. Corrections are needed for the relative distance (B) and the off axis directionality (C). Therefore

$$\left[ \begin{array}{c} \text{SCATTERING} \\ \text{LOSS} \end{array} \right]_{\text{dB}} = A + B + C + 6 \text{ dB} \quad (22)$$

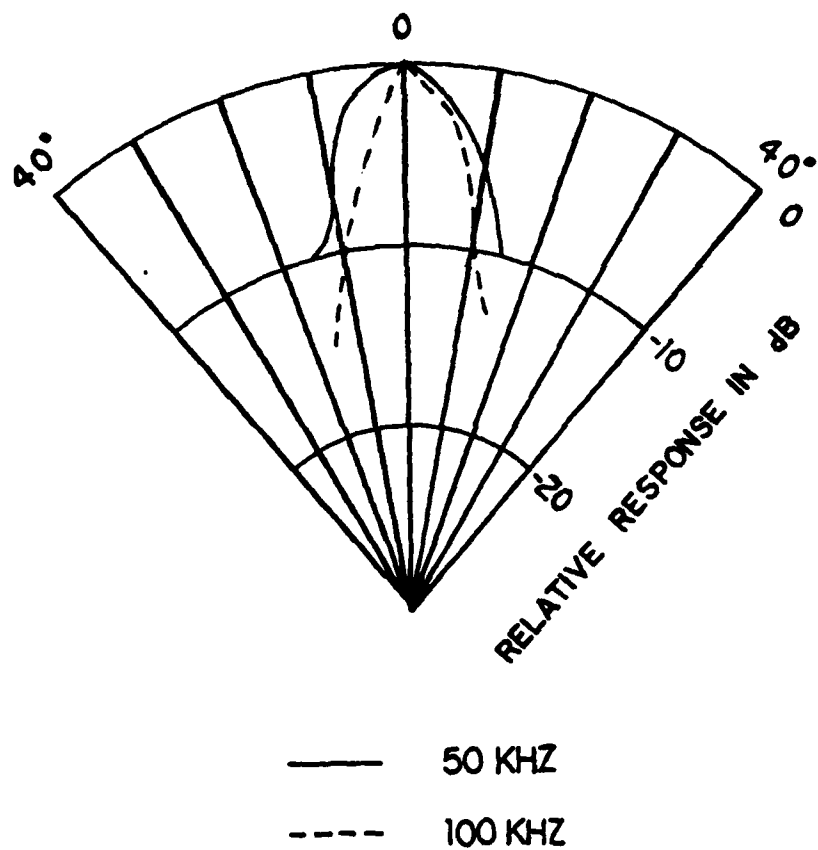


Figure 35. Beam pattern for dielectric transducer

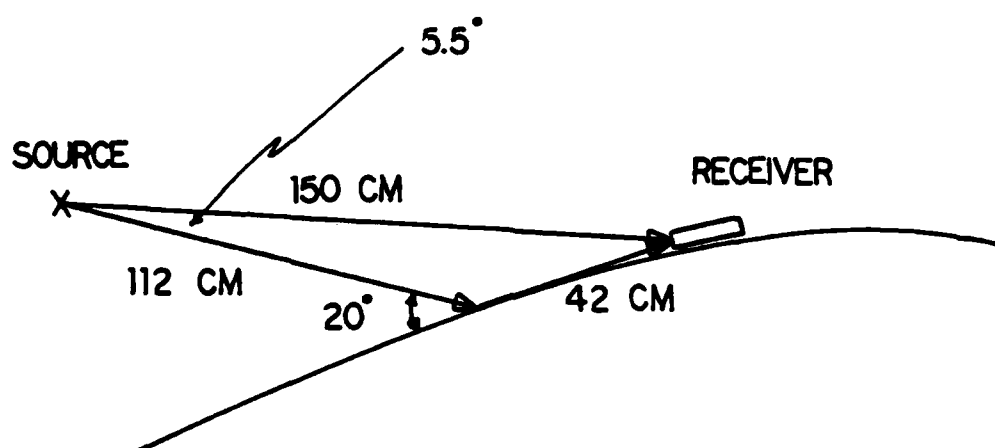


Figure 36. Geometry of the forward scatter measurement

where

$$A = 20 \text{ LOG } \left[ \frac{V_{\text{DIRECT}}}{V_{\text{SCATTERED}}} \right]$$

$$B = 20 \text{ LOG } \left[ \frac{R_{\text{DIRECT}}}{R_{\text{SCATTERED}}} \right]$$

$$C = \text{dB DOWN AT } 5.5^\circ$$

E.g., scattering loss at 50 kHz = -4.8 -2.8 -1.5 +6.0 = -3.1 dB. A correction of +6 dB is required since there is a pressure doubling at the rigid boundary of the model surface which is part of the scattered energy. This results in a forward scattering gain of approximately +3.1 dB at 50 kHz and + 6.3 dB at 100 kHz.

It should be recognized that using a pulsed signal results in a "snapshot" of the scattered signal. To get an accurate measure of the scattered energy using CW at sea, a CW signal should be used in the laboratory. This would in effect integrate the reverberation over a suitable time. It is presumed that the peak forward scatter found using the pulsed signal is close to the true scatter. A computer study is presently underway to resolve this problem, but the results were not available at the time of this writing.

The degree of forward scatter here is a function of what could be called the mesoscale roughness. The modeled

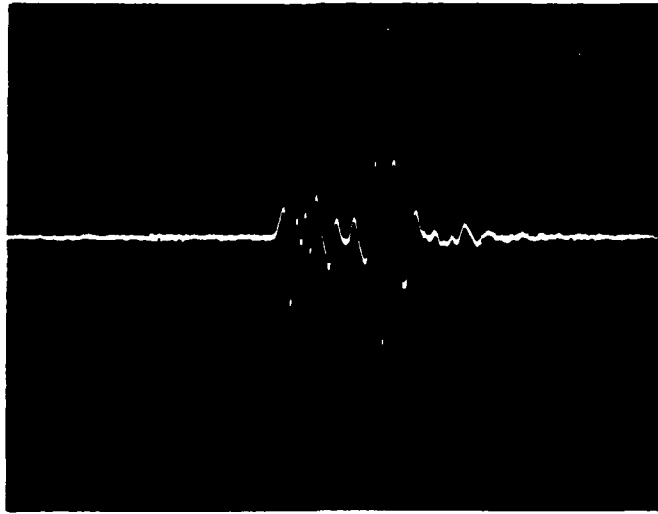


Figure 37. Oscilloscope display of direct path and forward scattered signal; 1v/cm, 100 $\mu$ s/cm,  $f = 50$  kHz.

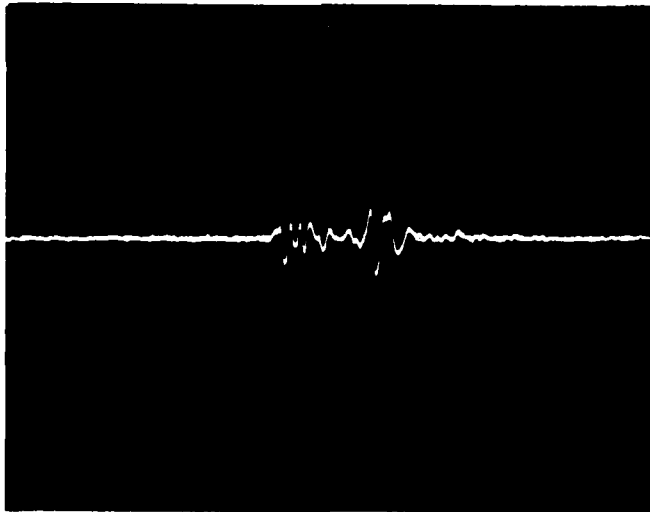


Figure 38. Oscilloscope display of direct path and forward scattered signal; 1v/cm, 100 $\mu$ s/cm,  $f = 100$  kHz.

surface reproduced the bathymetric readings to increments of 25M of depth in the ocean. This is equivalent to  $1/8''$  on the model and is approximately the wavelength in air of a 100 kHz signal. It is assumed that the scattered energy is not particularly sensitive to the unknown fine, local roughness of order less than one wavelength at the intercept point on the seamount; but rather it is most affected by the mesoscale roughness along the entire travel path along the slope.

## 2. Measurement Of Diffraction Loss

It is the seamount surface-scattered energy, traveling over the upslope surface, that diffracts over the crest. Therefore, the at-sea situation was experimentally modeled with the source on the surface of the 3D model.

Receiver orientation was based on those rays that arrive at the receiver after diffraction. Since the DSS is strongly dependent on  $\theta$ , this is a critical decision. This orientation was determined by making the assumption that the crest of the seamount acts as a reradiation line for the diffracted energy. By designating the crest as a sound source, a ray trace program was run by Fleet Numerical Weather Central in Monterey to ascertain what rays arrive at the receiver. From Figure 39 it can be seen that only two rays intercept the receiver at the 329M depth at 60 km range: the  $+2^\circ$  and  $-6^\circ$  rays measured with respect to the horizontal at the crest.

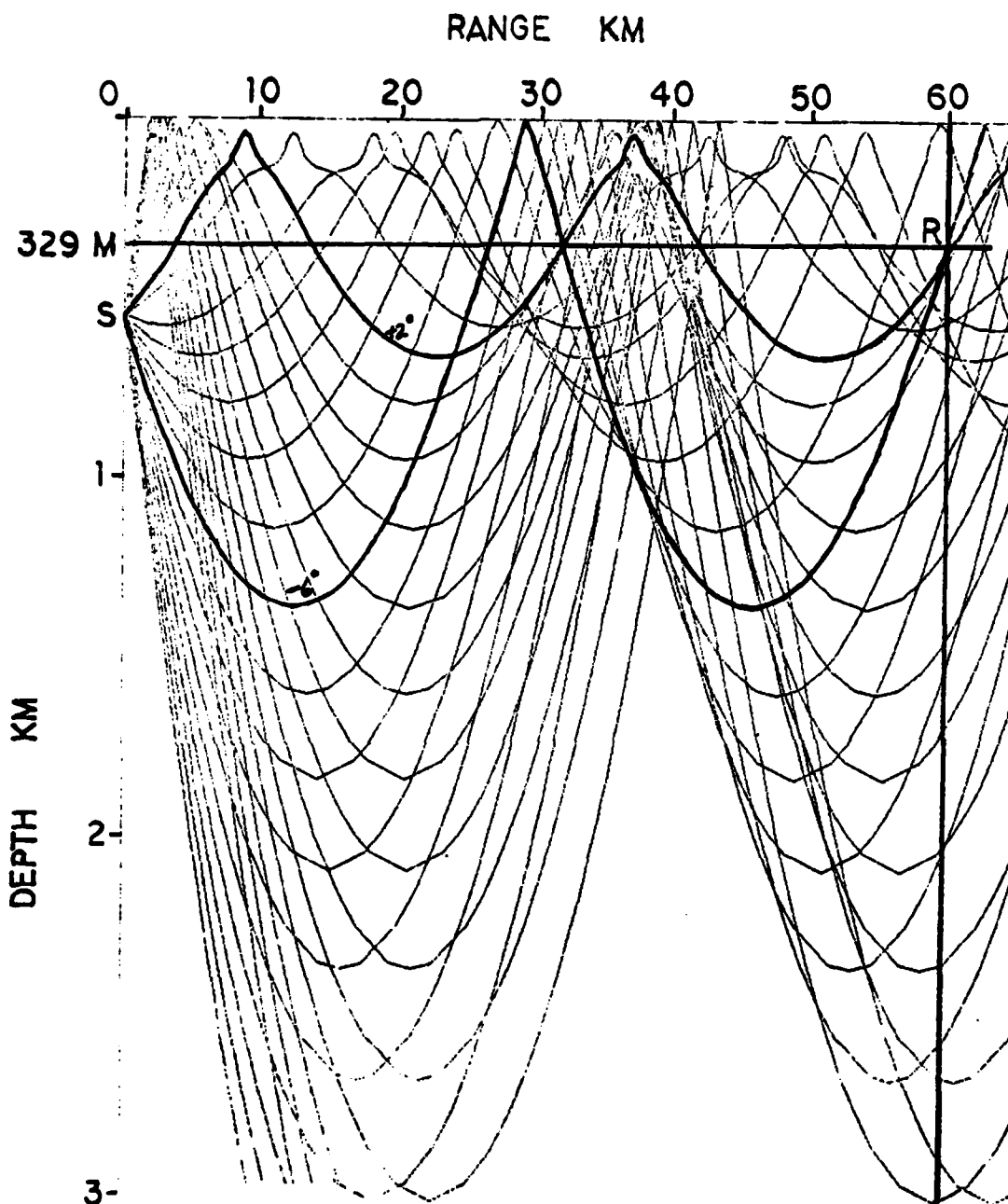


Figure 39. Ray tracings with seamount crest designated at the source.  
Receiver depth = 329 m.

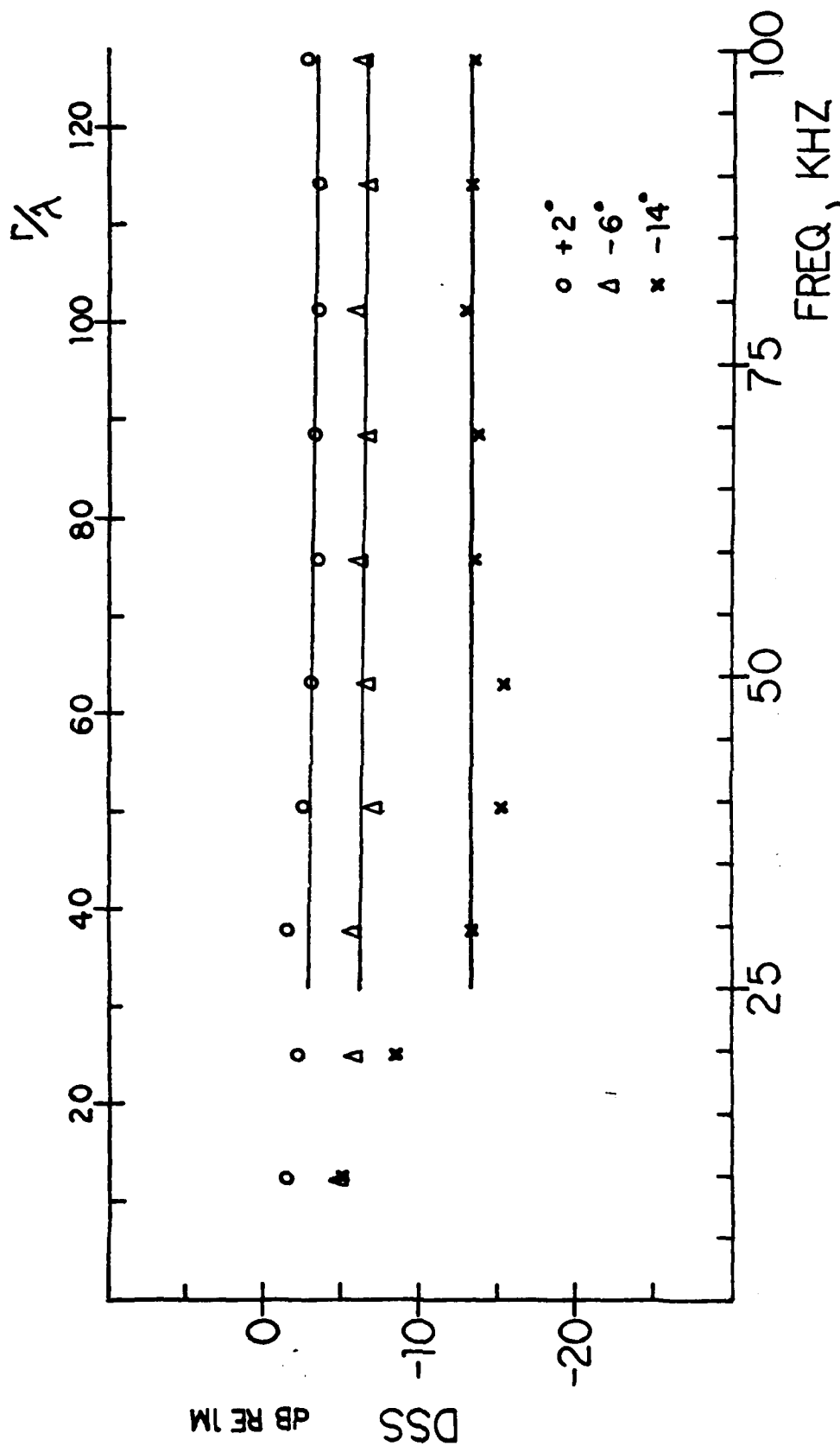


Figure 40. Diffraction scattering strength for 3D model as a function of receiver angle with respect to the horizontal;  $r_0 = r = 45$  cm (3.54 km),  $\theta_0 = 0$ .



The diffraction loss experiment was set up with  $r_0 = r = 45$  cm (3.45 km at sea), which is close to the midpoint of the upslope;  $\theta_0 = 0$ , and  $\theta = +2^\circ$ ,  $-6^\circ$ , and  $-14^\circ$  with respect to the horizontal. Figure 40 illustrates the resultant DSS. The DSS for  $\theta = +2^\circ$  is asymptotic at  $-3.0 \pm 0.5$  dB and for  $\theta = -6^\circ$  the asymptote is  $-6.0 \pm 0.5$  dB.

As can be seen the DSS is constant for  $r/\lambda > 40$ . At the upper ray intercept point to crest range,  $r_0$  at sea, we have  $r/\lambda = 543$ . Therefore, utilizing both DSS asymptotes in equation 21, the diffraction loss is  $+24 \pm 0.5$  and  $+27 \pm 0.5$  dB for the  $+2^\circ$  and  $-6^\circ$  rays respectively,  $r_0 = r = 3.54$  km at 230 Hz.

### 3. Computation Of The Refraction Losses

The first propagation loss computed using the FACT model was the refraction loss between source and seamount surface at the point where  $r_0 = 3.54$  km the individual rays intercepting the seamount were run through the program. The average propagation loss was found to be +76 dB re 1M with a  $\pm 2$  dB variation depending on the ray angle.

The computation of the additional refraction loss from seamount to receiver was complicated by the fact that the  $+2^\circ$  and  $-6^\circ$  rays from the crest do not originate at the source reference position for propagation loss. To solve this problem, the sound source identified in the computer program was set at the correct range (19 km from the crest) but displaced in depth to allow the generation of grazing rays of  $+2^\circ$  and  $-6^\circ$  outgoing from the crest. The difference

in propagation loss to a range beyond the crest equal to  $r$  (3.54 km) and to the receiver is then the required additional propagation loss necessary to account for the total propagation loss on both sides of the seamount. By this method the additional propagation loss was determined to be +6 dB for the  $+2^\circ$  ray and +12 for the  $-6^\circ$  ray.

#### 4. Total Propagation Loss

The contributing propagation losses are given in the following table:

	<u><math>+2^\circ</math> ray</u>	<u><math>-6^\circ</math> ray</u>
Propagation loss from source to seamount upslope at $r = 3.54$ km (for the range of incident rays)	$+76.0 \pm 2$ dB	$+76.0 \pm 2$ dB
Rough surface scattering loss at upslope	-6.3 dB	-6.3 dB
Diffraction loss over crest at $r_0 = r = 3.54$ km	$+24.0 \pm 0.5$ dB	$+27.0 \pm 0.5$ dB
Additional propagation loss from $r = 3.54$ km beyond crest to receiver	<u>+6.0 dB</u>	<u>+12.0 dB</u>
Total Propagation Loss	$+109.3 \pm 2.5$ dB	$+100.3 \pm 2.5$ dB

The contribution of the two arriving rays at the receiver may be summed, on the assumption that the energy is incoherent, to yield the total predicted propagation loss of  $+99.3 \pm 2.5$  dB re 1M. For comparison, from Figure 6 the at-sea propagation loss in the fully blocked case is  $+98 \pm 5$  dB re 1M.

## VII. CONCLUSIONS

Experimental investigation of the nature of diffraction over complex barriers can be accomplished in the laboratory using physical models.

The new concept of dimensionless diffraction scattering strength has been shown to be effective in determining range and frequency dependent diffraction loss from a scale model.

The laboratory prediction of long range propagation loss was found to be within 1 dB of the propagation loss measured by Ebbeson, et al., at Dickens Seamount. With proper mesoscale surface detailing of three dimensional models, it has been demonstrated that accurate predictions of at-sea shadowing loss can be obtained.

## BIBLIOGRAPHY

1. Biot, M.A. and Tolstoy, I., "Formulation Of Wave Propagation In Infinite Media By Normal Coordinates With An Application To Diffraction", The Journal Of The Acoustical Society Of America, V. 29, p. 381 - 391, 1957.
2. Bremhorst, J.H., "Impulse Wave Diffraction By Rigid Wedges and Plates", M.S. Thesis, U.S. Naval Postgraduate School, Monterey, Ca., 1978.
3. Tolstoy, I., Wave Propagation, McGraw-Hill, 1973.
4. Medwin, H., "Computer Modeling Of Diffraction By Complex Barriers," in paper preparation.
5. Ebbeson, G.R., Thorleifson, J.M. and Turner, R.G., "Shadowing Of Sound Propagation By A Seamount In The North Pacific", The Journal Of The Acoustical Society Of America, V. 64, S(76), 1978
6. Frederiksen, E., "Condenser Microphones Used As Sound Sources", Bruel & Kjaer Technical Review, No. 3, 1977.

INITIAL DISTRIBUTION LIST

1. Defense Documentation Center Cameron Station Alexandria, Virginia 22314	2
2. Library, Code 0142 Naval Postgraduate School Monterey, California 93940	2
3. Department Chairman, Code 61 Department of Physics and Chemistry Naval Postgraduate School Monterey, California 93940	2
4. Professor H. Medwin, Code 61Md Department of Physics and Chemistry Naval Postgraduate School Monterey, California 93940	6
5. Lt. Robert P. Spaulding 11 Wisk-key Wind Road Wallingford, Connecticut 06492	1
6. Manager, Anti-Submarine Warfare Systems Project Office, (ASW 13) Attn: CDR. J. Hagy Department of the Navy Washington, D.C. 20362	1
7. Office Of Naval Research Arlington, Virginia 22217 Attn: Code 480 Attn: Dr. M. McKisic (Code 486) Attn: Code 460 Attn: Code 102-05	3 1 1 1
8. Mr. G.R. Ebbeson Defense Research Establishment Pacific F.M.O. Victoria, British Columbia, VOS 1 60 Canada	1
9. Professor R.H. Bourke, Code 68Bf Department of Oceanography Naval Postgraduate School Monterey, California 93940	1

10. Naval Research Laboratory  
Washington, D.C. 20375  
Attn: Mr. Henry Fleming, Code 8106 1  
Attn: Mr. Burton G. Hardie 1
11. Ms. Joan Bertrand, Code 320 1  
Naval Electronics Systems Command  
Washington, D.C. 20360
12. Chairman, Department of Oceanography, Code 68 1  
Naval Postgraduate School  
Monterey, California 93940
13. Mr. Melvin A. Peterson, Code 724 1  
Naval Ocean Systems Center  
San Diego, California 92152
14. Dr. I. Tolstoy 1  
Knockvennie  
Castle Douglas, KIRKS  
Scotland, United Kingdom
15. Commander  
Naval Oceanographic Office  
Washington, D.C. 20390  
Attn: Code 1640 1  
Attn: Code 70 1
16. Director of Defense Research and Engineering  
Office of the Secretary of Defense  
Washington, D.C. 20301  
Attn: Office of Assistant Director for Research 1
17. Naval Ocean Research and Development Activity  
NSTL Station, Mississippi 39529  
Attn: Dr. Gerald Morris (Code 200) 1  
Attn: Dr. Aubrey L. Anderson 1
18. Naval Underwater Systems Center  
Fort Trumbull  
New London, Connecticut 06320  
Attn: Mr. David G. Browning (Code 3121) 1
19. Defense Advanced Research Projects Agency 1  
1400 Wilson Blvd.  
Arlington, Virginia 22207
20. Dr. J.C. Novarini 1  
Ave. Cordoba 1180  
Cap. Fed. 1180  
Buenos Aires, Argentina
21. Professor O.B. Wilson, Code 61W1 1  
Department of Physics and Chemistry  
Naval Postgraduate School  
Monterey, California 93940